



Scaling up the Single Transducer Thickness-Independent Ultrasonic Imaging Method for Accurate Characterization of Microstructural Gradients in Monolithic and Composite Tubular Structures

Don J. Roth, Dorothy V. Carney, and George Y. Baaklini
Lewis Research Center, Cleveland, Ohio

James R. Bodis and Richard W. Rauser
Cleveland State University, Cleveland, Ohio

National Aeronautics and
Space Administration

Lewis Research Center

Available from

NASA Center for Aerospace Information
800 Elkridge Landing Road
Linthicum Heights, MD 21090-2934
Price Code: A03

National Technical Information Service
5287 Port Royal Road
Springfield, VA 22100
Price Code: A03

SCALING UP THE SINGLE TRANSDUCER THICKNESS-INDEPENDENT ULTRASONIC IMAGING METHOD FOR ACCURATE CHARACTERIZATION OF MICROSTRUCTURAL GRADIENTS IN MONOLITHIC AND COMPOSITE TUBULAR STRUCTURES

Don J. Roth, Dorothy V. Carney, George Y. Baaklini
National Aeronautics and Space Administration
Lewis Research Center
Cleveland, Ohio 44135

and

James R. Bodis, Richard W. Rauser
Cleveland State University
Cleveland, Ohio 44115

SUMMARY

Ultrasonic velocity/time-of-flight imaging that uses back surface reflections to gauge volumetric material quality is highly suited for *quantitative* characterization of microstructural *gradients* including those due to pore fraction, density, fiber fraction, and chemical composition variations. However, a weakness of conventional pulse-echo ultrasonic velocity/time-of-flight imaging is that the image shows the effects of thickness as well as microstructural variations unless the part is uniformly thick. This limits this imaging method's usefulness in practical applications. Prior studies have described a pulse-echo time-of-flight-based ultrasonic imaging method that requires using a single transducer in combination with a reflector plate placed behind samples that eliminates the effect of thickness variation in the image. In those studies, this method was successful at isolating ultrasonic variations due to material microstructure in plate-like samples of silicon nitride, metal matrix composite, and polymer matrix composite. In this study, the method is engineered for inspection of more complex-shaped structures—those having (hollow) tubular/curved geometry. The experimental inspection technique and results are described as applied to (1) monolithic multi-layer ceramic and polymer matrix composite “proof-of-concept” tubular structures that contain machined patches of various depths and (2) as-manufactured monolithic silicon nitride ceramic and silicon carbide/silicon carbide composite tubular structures that might be used in “real world” applications.

BACKGROUND

Prior studies have shown that ultrasonic velocity/time-of-flight imaging that uses back surface echo reflections to gauge volumetric material quality is well suited (perhaps more so than is the commonly-used peak amplitude c-scanning) for *quantitative* characterization of microstructural *gradients*. Such gradients include those due to pore fraction, density, fiber fraction, and chemical composition variations (fig. 1) (refs. 1 to 5). Variations in these microstructural factors can affect the uniformity of physical performance (including mechanical [stiffness, strength], thermal [conductivity], and electrical [conductivity, superconducting transition temperature], etc. performance) of monolithic and composite components (refs. 2 and 6 to 8). A weakness of conventional ultrasonic velocity/time-of-flight imaging (as well as to a lesser extent ultrasonic peak amplitude c-scanning where back surface echoes are gated (ref. 16)) is that the image shows the effects of thickness as well as microstructural variations unless the part is uniformly thick. This limits this type of imaging's usefulness in practical applications. The effect of thickness is easily observed from the equation for pulse-echo waveform time-of-flight (2τ) between the first front surface echo (FS) and the first back surface echo (B1), or between two successive back surface echoes where:

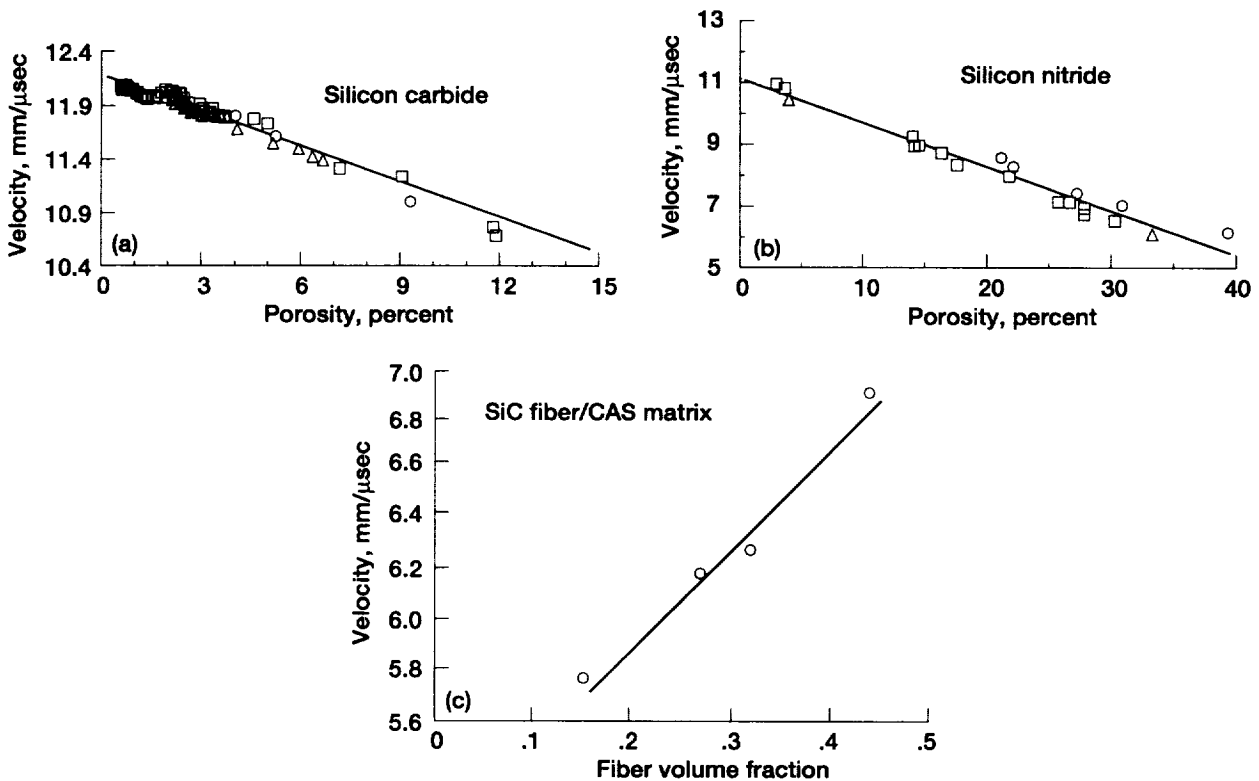


Figure 1.—Correlation of velocity with microstructural variation. (a) Velocity vs. percent porosity for silicon carbide. (b) Velocity vs. percent porosity for silicon nitride. (c) Velocity vs. fiber volume fraction for SiC/CAS ceramic matrix composite.

$$2\tau = \frac{(2d)}{V} \quad (1)$$

where d is the sample thickness and V is the velocity of ultrasound in the material. Interpretation of the time-of-flight image is difficult as thickness variation effects can mask or overemphasize the true microstructural variation portrayed in the image of a part containing thickness variations. Thickness effects on time-of-flight can also be interpreted by rearranging equation (1) to calculate velocity:

$$V = \frac{(2d)}{(2\tau)} \quad (2)$$

such that velocity is inversely proportional to time-of-flight. Velocity and time-of-flight maps will be affected similarly (although inversely in terms of magnitude) by thickness variations, and velocity maps are used in this investigation to indicate time-of-flight variations.

THICKNESS-INDEPENDENT ULTRASONIC VELOCITY MEASUREMENTS

Several attempts to account for thickness variation effects in ultrasonic velocity measurements were noted in the literature. One study (ref. 9) used two transducers located on opposite sides of the sample (fig. 2(a)). Accurate thickness (d) at each scan location was obtained via both transducers using the time-of-flights (t_1 , t_2) acquired from pulse-echo front surface reflections off both surfaces of the sample, and using the known constant velocity in water (c) and the known distance (D) between the two transducers according to:

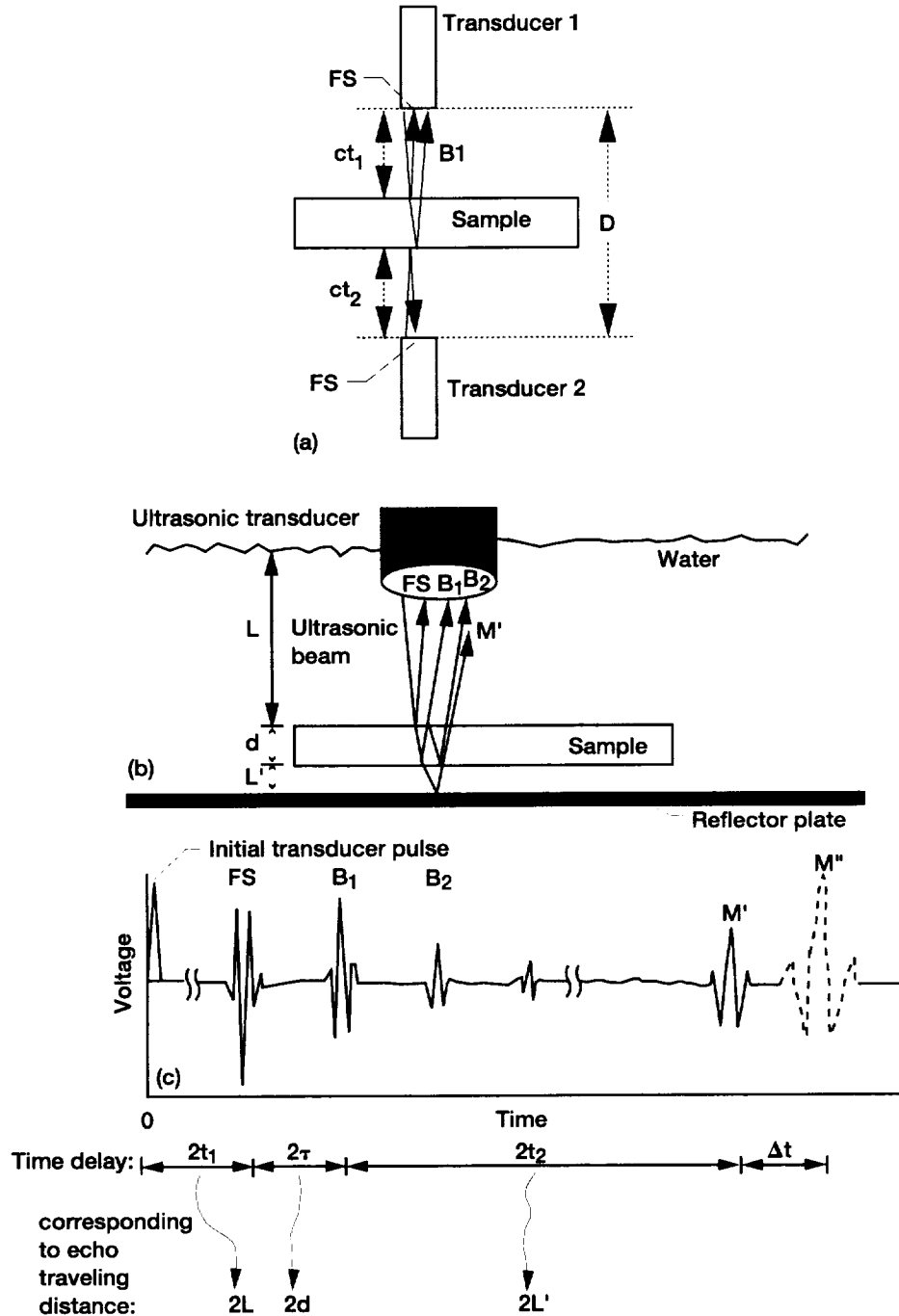


Figure 2.—Two methods for obtaining thickness-independent velocity. (a) Two-transducer method. D = distance between transducers, c = velocity of ultrasound in water, t_1 and t_2 = the time-of-flights acquired from pulse-echo front surface reflections off both surfaces of the sample. Thickness is determined from eq. (3). Pulse-echo time-of-flight (2τ) between the first front surface echo (FS) and the first back surface echo (B1) is obtained by one of the transducers at each scan location. Knowing thickness (d) and time-of-flight (2τ) at each scan location, thickness-independent velocity (V) images were calculated according to eq. (2). (b) Single transducer reflector plate method used in this investigation. (c) Resulting waveforms from method in (b).

$$d = D - ct_1 - ct_2 \quad (3)$$

Additionally, pulse-echo time-of-flight (2τ) was obtained by one of the transducers at each scan location by acquiring the pulse-echo time delay between a front and back surface echo or between two successive back surface echoes. Knowing thickness (d) and pulse-echo time-of-flight (2τ) at each scan location, thickness-independent velocity (V) images were calculated according to equation (2).

Several studies (refs. 10 to 13) described a single point ultrasonic velocity measurement method using a reflector plate located behind and separated from the sample, that does not require prior knowledge of sample thickness. The latter method was studied with success in prototypical scanning configurations for plate-like shapes, (refs. 14 to 16) and incorporated into a commercial scan system (refs. 16 and 17). Figure 2(b) shows a schematic of the immersion pulse-echo testing set-up required to use this method and the resulting ultrasonic waveforms. The mathematical derivation for the method (ref. 16) results in ultrasonic velocity being calculated according to

$$V = c \left(\frac{\Delta t}{2\tau} + 1 \right) \quad (4)$$

where c is water velocity, 2τ is the pulse-echo time-of-flight as previously defined, and Δt is the pulse-echo time-of-flight difference between the first echo off the reflector plate front surface with and without the sample present, respectively. Water velocity (c) is determined from known relations between water velocity and temperature (ref. 18) or by direct measurement using the time difference of ultrasonic wave travel between two transducer linear positions. This thickness-independent ultrasonic imaging method does not require prior knowledge of sample thickness as shown in equation (4) and if engineered for scanning, the effect of thickness variation is eliminated in the resulting image. Precision and relative accuracy associated with this method are estimated at near 1 percent for plate-like samples having machined surfaces (ref. 16). The thickness-independent methods noted here (refs. 9 to 17) require access to both sides of the sample, i.e., there is not a single-sided technique available for scanning that will result in thickness-independence.

SCOPE OF INVESTIGATION

In this investigation, the single transducer reflector plate method shown in figure 2 was scaled-up/engineered for tubular-shaped structures, and the results are presented. The method was used to inspect (1) monolithic mullite ceramic and polymer matrix composite "proof-of-concept" tubular structures that contained machined patches of various depths and (2) as-manufactured monolithic silicon nitride ceramic and silicon carbide/silicon carbide composite tubular structures that might be used in "real world" application. Thickness-independent ultrasonic images for these materials are compared to conventional (apparent) pulse-echo velocity images (the latter being obtained using eq. (2)). The single transducer reflector plate method (refs. 10 to 17) was chosen over the two-transducer method (ref. 9) because of its simplicity and the fact that some tubes under investigation at NASA for high temperature structural duty have inner regions too small to contain a perpendicularly-positioned second transducer but still large enough to contain a reflector plate. The silicon nitride tube is an examples of such a tube.

EXPERIMENTAL

Basic Procedure

The thickness-independent ultrasonic imaging method requires at least two scans to collect the necessary time-of-flight information (entire echoes, or times to echo peaks or edges—see the Appendix for a discussion of timing issues) (fig. 3). The first of the two scans is run with the sample in place and the time-of-flight information associated with echoes FS (front surface echo), B1 (first back surface echo), B2 (second back surface echo), and M' (first echo off reflector plate front surface with sample present) is collected. Following this, the sample is removed and a second scan is run to collect the time-of-flight information associated with M'' (first echo off reflector plate front surface with sample removed). In this investigation, three scans were used to obtain all echo time-of-flight informa-

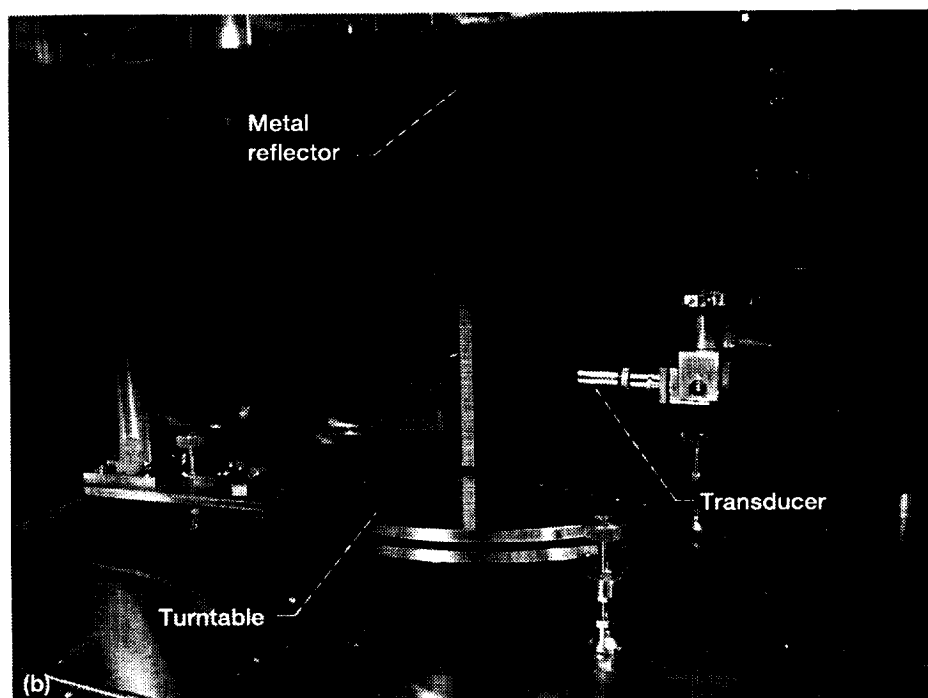
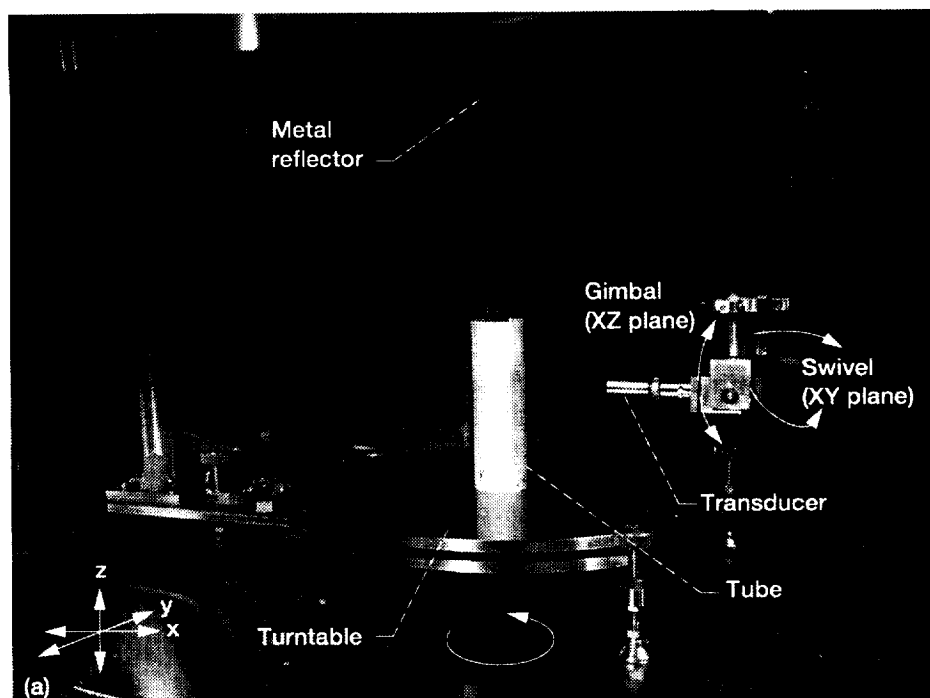


Figure 3.—Ultrasonic scan set-up using turntable scan to obtain thickness-independent velocity images. (a) Scan 1: sample present, collect B1, B2, M'. (b) Scan 2: sample removed, collect M".

tion as required using the version of this method that is commercially-available (ref. 17). FS and B1, or B1 and B2 time-of-flight information were obtained in scan 1, M' time-of-flight information was obtained in scan 2 and M'' time-of-flight information was obtained in scan 3. Echo cross-correlation during the first scan, or times to echo peaks and/or edges during any of the scans, were used to obtain time delays 2τ and Δt (eq. (4)). Entire echo digitization and storage was not required in this investigation as it was in reference 15. (Obtaining timing information in this manner resulted in slower scan speed but a major reduction in storage required, near-instantaneous velocity image calculation, and more flexibility in capturing desired echo feature times as compared to that for reference 15. For best absolute accuracy, it is still recommended that all waveforms be digitized and stored and subsequent time delay calculated using cross-correlation.) As shown in figure 3(a), a tube was placed upon a motorized turntable assembly placed in the immersion scan tank. A machined stainless steel or brass reflector plate was suspended from the scanner bridge and positioned internal to the tube approximately 1 cm from the inside wall. In this manner, the reflector plate remained stationary throughout the scan. Prior to the scan, the transducer was positioned perpendicularly to the tube front surface using lateral, gimbal and swivel adjustments to obtain highest front surface reflection near the scan start position. Then, the distance between the transducer and tube was adjusted starting from the focal length to that distance where tube back surface echoes and reflector echoes were highest. The scanning proceeded as follows. The turntable spun so that one scan line corresponded to a full rotation (360°) of the tube. Ultrasonic data was obtained every 1° . After the turntable completed a full rotation and thus returned to the scan starting position, the transducer was stepped up in height 1 mm so that a new 360° line of data could be obtained. Images were contrast-expanded to better reveal *global* material variation by replacing relatively high and/or low (abnormal) data values that occurred in very low numbers with overall average values that occurred in the original image. Color schemes for the specific images were chosen based on optimum viewing of variations for the examiner but all contained 235 discrete levels.

Material Description and Experimental Parameters

Table I describes each tubular sample and the experimental scan parameters used to obtain the apparent and thickness-independent ultrasonic velocity images for each sample. Figure 4 shows photographs of the tubes. All transducers were the spherically-focused, longitudinal wave type. Scan and step increment were 1 deg and 1 mm, respectively. The echo features (entire echo, leading edges, peaks) used to obtain differences in time-of-flight (DTOF) 2τ and Δt (eq. (4)) were acquired during the scan and optimized for each sample tube based on the characteristics of the echoes. Analog-to-digital sampling rate was 250 MHz providing a time resolution of 4 nsec. See the Appendix for a discussion of timing issues.

Additional Experimental Study

All tubes were measured for wall thickness at various locations (including all machined patches) using calipers and/or micrometers. X-ray computed tomography (CT) was performed at several cross-sectional locations of the monolithic ceramic silicon nitride to examine for variations in thickness and microstructural features such as density/pore fraction that might correlate with velocity variations seen in the apparent and thickness-independent ultrasonic image. CT set-up was as follows. Slice locations were at 1, 5, 25, 50, 75, 80, 85, 100, and 125 mm from the top surface of the silicon nitride tube. Test Parameters were 160 kV, 200 mA, 1000 ms exposure time, 0.5 degree scan increment (720 views/slice), and 3 position radial scan (3 positions needed since beam width less than ceramic tube diameter). The source-to-object distance and source-to-detector distance were 60 and 105 mm, respectively. The reconstructed pixel size was 0.05 mm. Region-based contrast expansions were performed on images to optimize viewing of any nonuniformity. CT slices encompassed 0.2 mm of material thickness.

Conventional film radiography through the thickness of the silicon nitride tube was also performed at selected locations with the film placed against the inside diameter of the tube. Parameters for the film radiography were tube voltage = 45 kV, current = 7 ma, 0.7 mm focal spot, exposure time = 3 min, source-to-film distance = 91 cm, and use of M film. X-ray density (XD) at various locations of both tubes was determined from:

$$XD = \log \frac{I_0}{I_t} \quad (5)$$

TABLE I.—MATERIAL DESCRIPTION AND EXPERIMENTAL PARAMETERS FOR TUBULAR SAMPLES

Tube material and description	Experimental scan parameters	Echo features used for 2τ DTOF calculation method	Echo features used for Δt DTOF calculation method*
Mullite (silica-alumina) monolithic ceramic "proof-of-concept" sample. Nominal wall thickness 4.1 mm, 53 mm outside diameter, and 150 mm height. Five square 10×10 mm patches of depth ~0.1, 0.2, 0.3, 0.4, and 0.5 mm were machined out of the EXTERIOR surface of the mullite tube to create thickness variation of up to 12 percent in the tube. See figure 4(a).	<ul style="list-style-type: none"> 20 MHz transducer 360 deg \times 40 mm strip 	Time to B1, B2 echo leading edges at coincident positions (video mode). (fig. A2(a))	Time to M', M" echo leading edges at coincident positions (video mode).
Polymer Matrix Composite (PMC) "proof-of-concept" sample. Nominal wall thickness 4.1 mm, 152 mm outside diameter, and 176 mm height. Five square 25×25 mm patches of depth ~0.1, 0.2, 0.3, 0.5, and 0.8 mm were machined out of the INTERIOR surface of the PMC tube to create thickness variation of up to 20 percent in the tube. See figure 4(b).	<ul style="list-style-type: none"> 2.25 MHz transducer 360 deg \times 60 mm strip 	FS, B1 entire echoes, negative correlation. (fig. A2(e))	Time to M', M" echo absolute peak below 100 percent FSH (video mode).
Ceramic Matrix Composite (Silicon Carbide fiber within Silicon Carbide Matrix) for high temperature structural applications. Nominal wall thickness 2.2 mm, 175 mm outside diameter, and 215 mm height. It was manufactured with up to ~0.4 mm thickness variation (approximately 15 percent of total thickness) due to the fiber weave pattern, grooving, and seaming. See figure 4(c).	<ul style="list-style-type: none"> 2.25 MHz transducer 360 deg \times 80 mm strip 	FS, B1 entire echoes, negative correlation. (fig. A2(e))	Time to M', M" echo absolute leading edge (video mode) at 20 percent FSH.
Silicon Nitride Monolithic Ceramic for high temperature structural application. Nominal wall thickness 7.5 mm, 48 mm outside diameter, and 150 mm height. It was manufactured unintentionally with a 0.8 mm thickness variation (approximately 10 percent of total thickness) and some microstructural variation. See figure 4(d).	<ul style="list-style-type: none"> 20 MHz transducer 360 deg \times 130 mm strip 	B1, B2 entire echoes, positive correlation. (fig. A2(c))	Time to M', M" echo (+)leading edge at (+)100 percent FSH (rf mode).

*FSH = Full Scale Height of the on-screen digital oscilloscope.

- video mode = rectified waveform, oscilloscope bounds = 0, 100 percent. See figure A2(a).

- rf mode = unrectified waveform, oscilloscope bounds = ± 100 percent. See figure A2(c).

where I_0 is the incident light intensity on the x-ray film negative and I_t is the transmitted light through the film.

CT and film radiography were followed by cutting the silicon nitride tube into several smaller tubular sections, metallographically polishing the surfaces of these, and examining for microstructural variations.

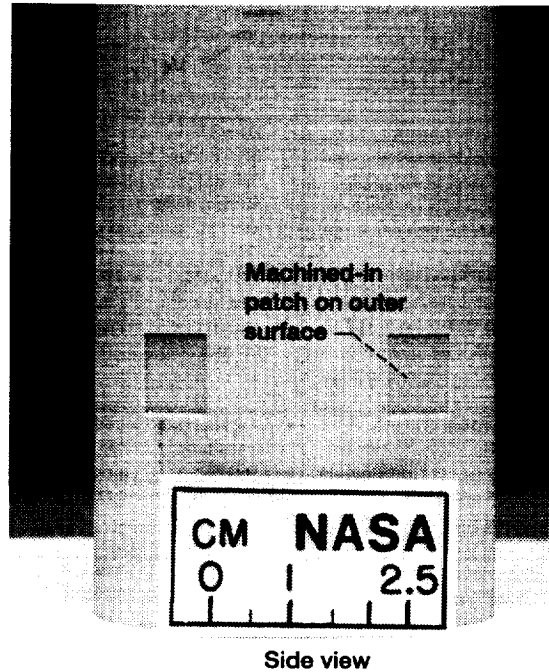
RESULTS AND DISCUSSION

General

Figures 5 to 10 show apparent velocity and thickness-independent velocity imaging results for the tubular structures. Most images are shown in "unwrapped" format, i.e., the tubular data is laid flat so that the entire 360° view can be seen. The histogram of velocity values is included near the image. Figures 9 and 10 show images as decaled onto tubular models; this type of representation is useful as well since the samples are tubular and a continuous fully-connected image is shown. Additionally, tubular views can be used to create animations of rotation. The percent variation in velocity rather than absolute velocity values is given as it is believed that this will have more value for the reader.

Proof-of-Concept Monolithic and Composite Tubes

Consider figures 5 and 6 where unwrapped images of apparent and thickness-independent velocity for 40 and 60 mm height slices, respectively, of the mullite and polymer matrix composite (pmc) tubes encompassing the machined-in patches are shown. The apparent velocity images of figures 5(a) and 6(a) clearly shows the patches with apparent velocity values increasing as material thickness decreases as expected based on equation (2). (Remember that the value of thickness (d) input for the calculation of the apparent velocity image remains constant while time delay 2τ is decreasing as the material thickness decreases.) Patch edges appear "stepped" due to the



(a)

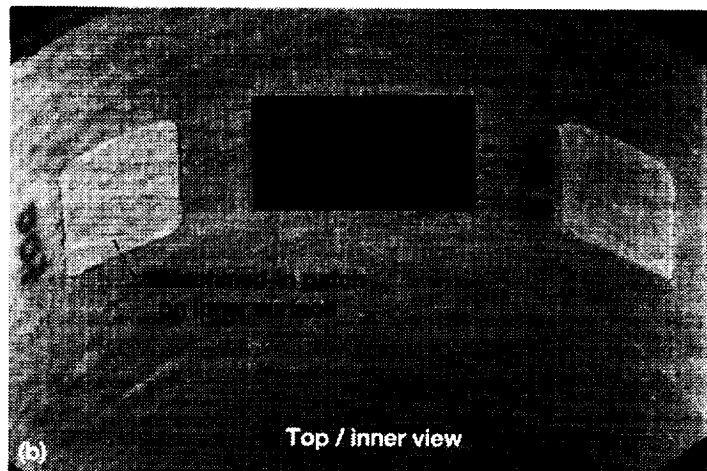
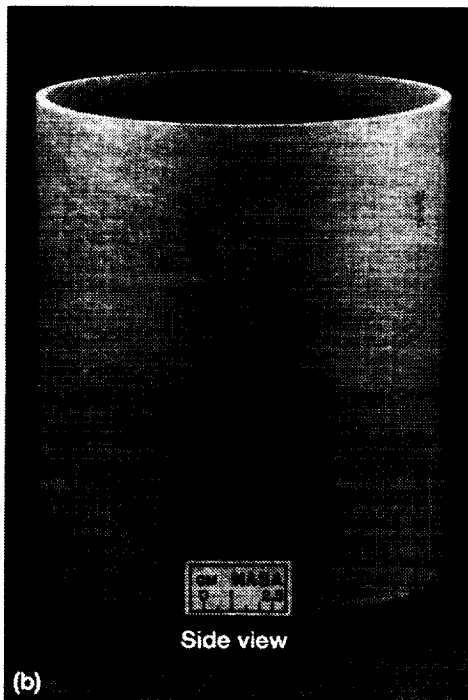


Figure 4.—Optical photographs of tubular structures. (a) Portion of monolithic Mullite Ceramic Tube with machined-in patches on the outer surface. Patch depths ~ 0.1, 0.2, 0.3, 0.4, and 0.5 mm. (b) Portion of Polymer Matrix Composite (PMC) Tube with machined-in patches on the inner surface. Patch depths ~ 0.1, 0.2, 0.3, 0.5, and 0.8 mm.

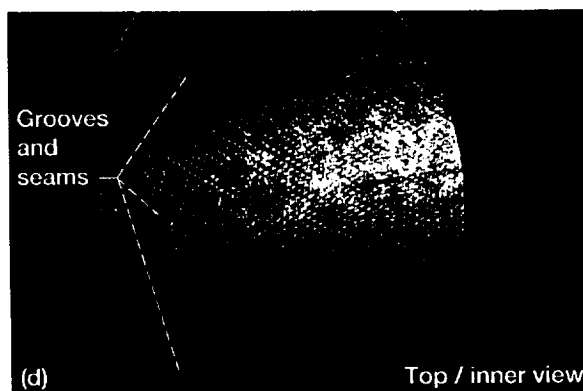
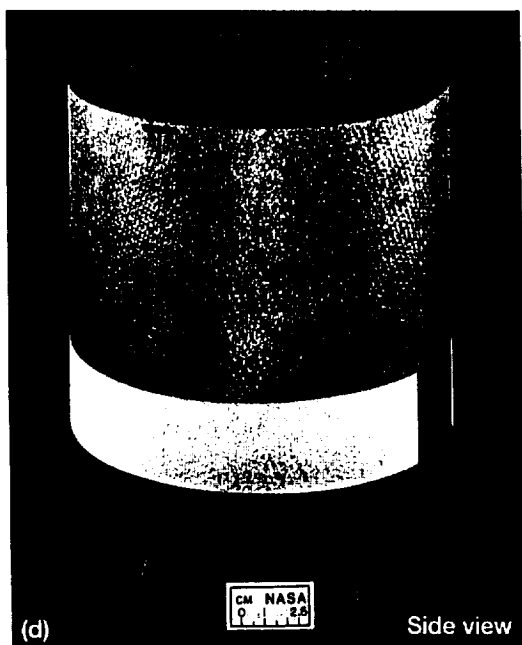
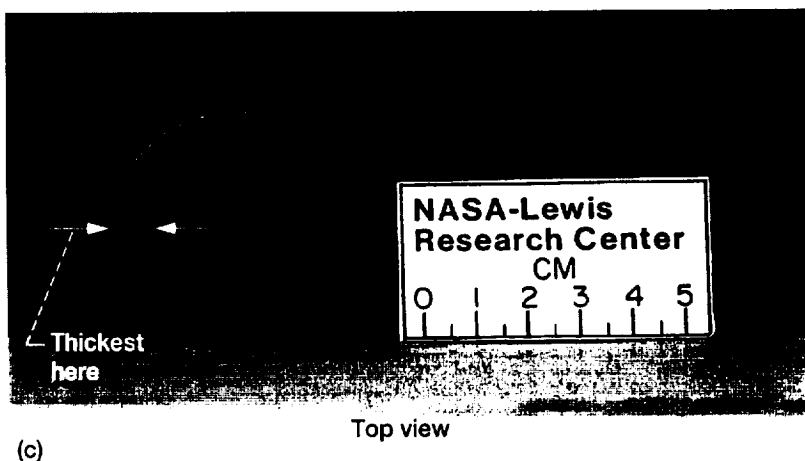
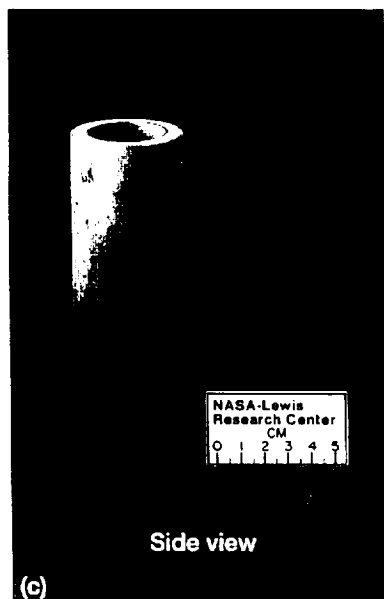


Figure 4.—Concluded. (c) Monolithic Silicon Nitride Ceramic Tube for High-Temperature Structural Application. Wall thickness ~ 800 μm thicker on one side vs. the other side towards the top of the tube (~ 10% thickness variation). (d) Silicon Carbide / Silicon Carbide Ceramic Matrix Composite Tube for High-Temperature Structural Application. The tube has variable thickness (up to ~ 15%) due to fiber weave architecture, interior grooving and seaming which complicates inspection process.

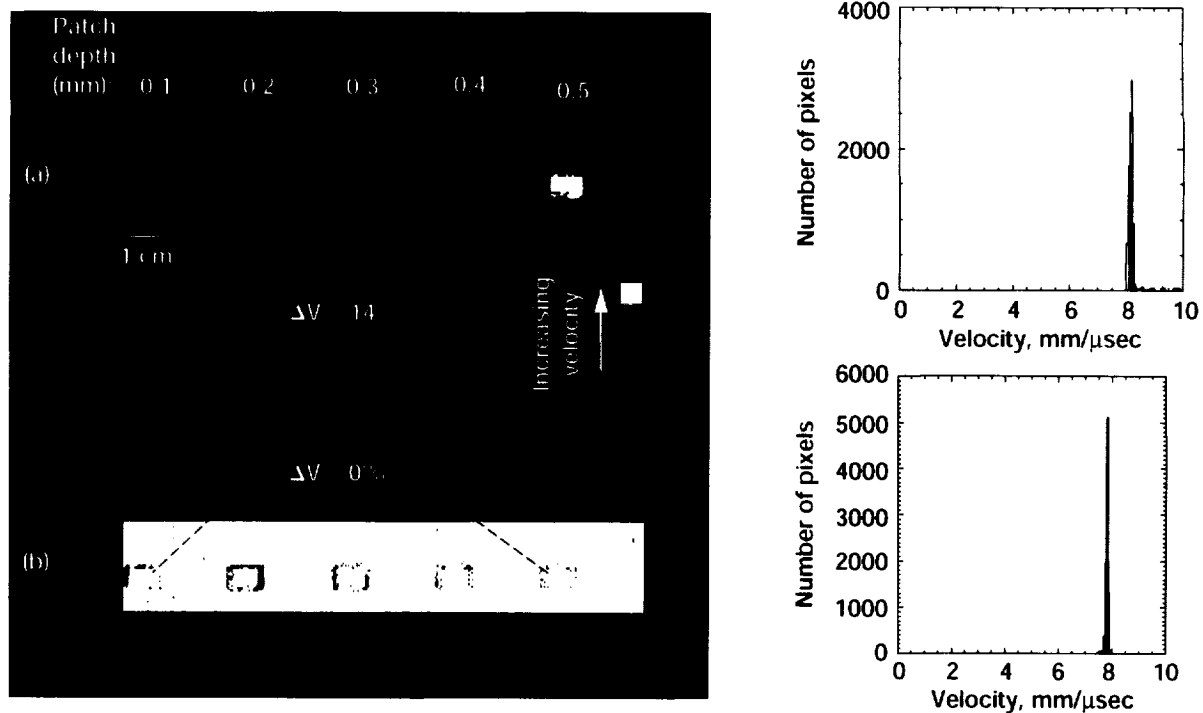


Figure 5.—Apparent and thickness-independent velocity images, and histograms of velocity values for a 40 mm height strip of mullite tube containing the machined-in patches. (a) Apparent velocity image. (b) Thickness-independent velocity image.

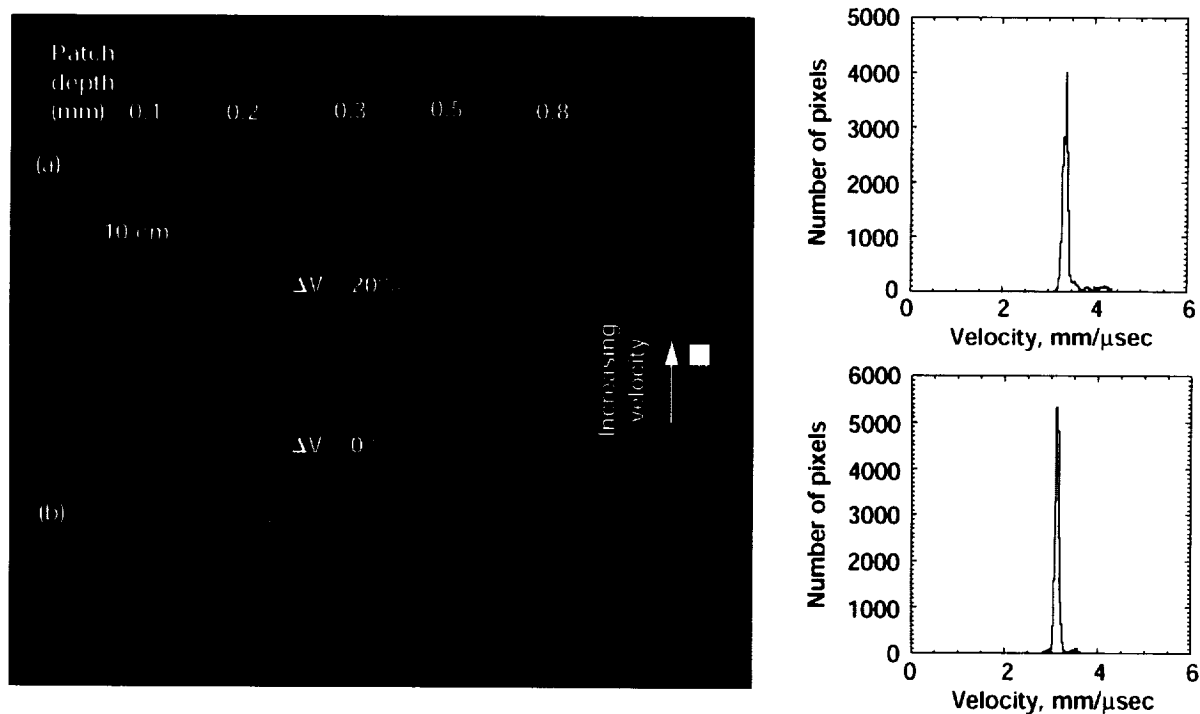


Figure 6.—Apparent and thickness-independent velocity images, and histograms of velocity values for a 60 mm height strip of polymer matrix composite tube containing the machined-in patches. (a) Apparent velocity image. (b) Thickness-independent velocity image.

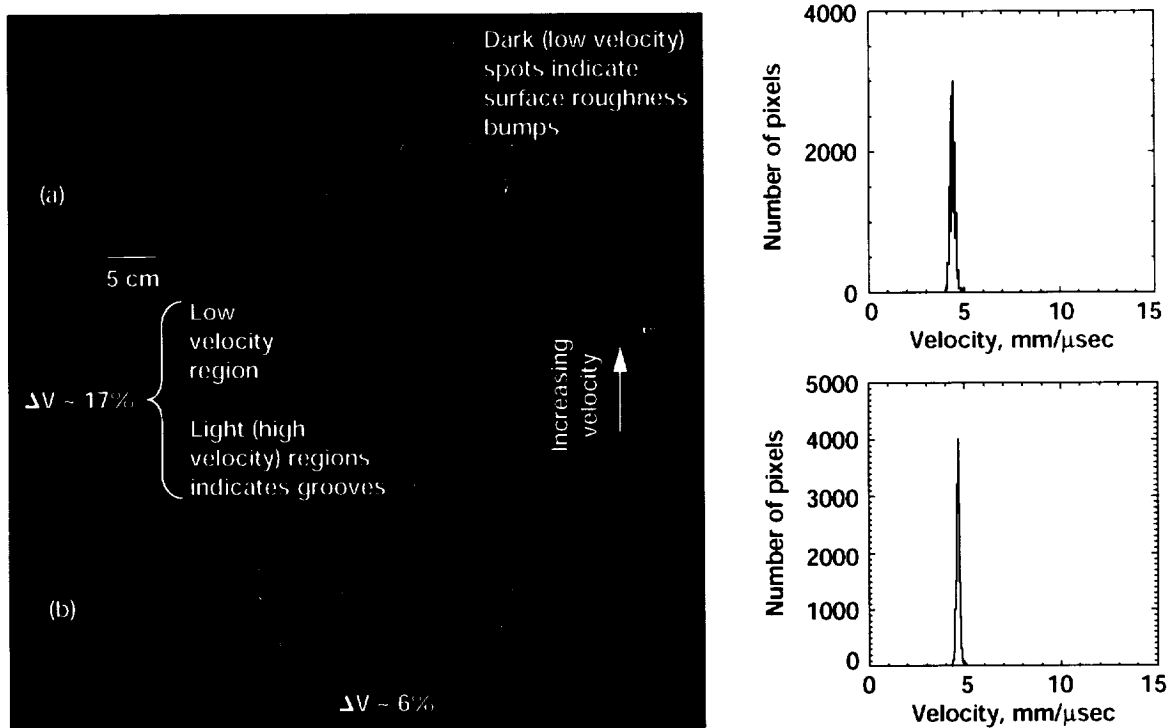


Figure 7.—Apparent and thickness-independent velocity images, and histograms of velocity values for a 100 mm height portion of the ceramic matrix composite (CMC) tube. (a) Apparent velocity image. (b) Thickness-independent velocity image.

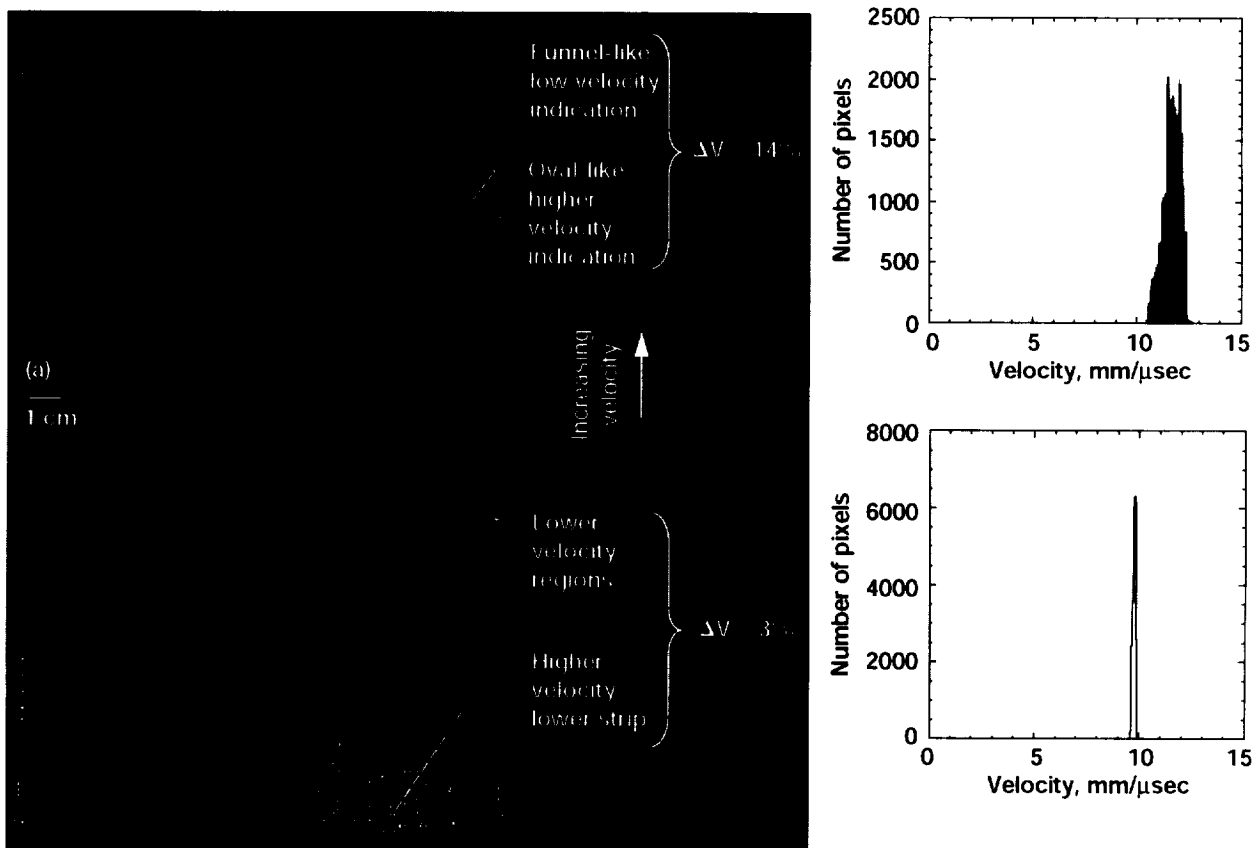


Figure 8.—Apparent and thickness-independent velocity images, and histograms of velocity values for a 130 mm height portion of the silicon nitride tube. (a) Apparent velocity image. (b) Thickness-independent velocity image.

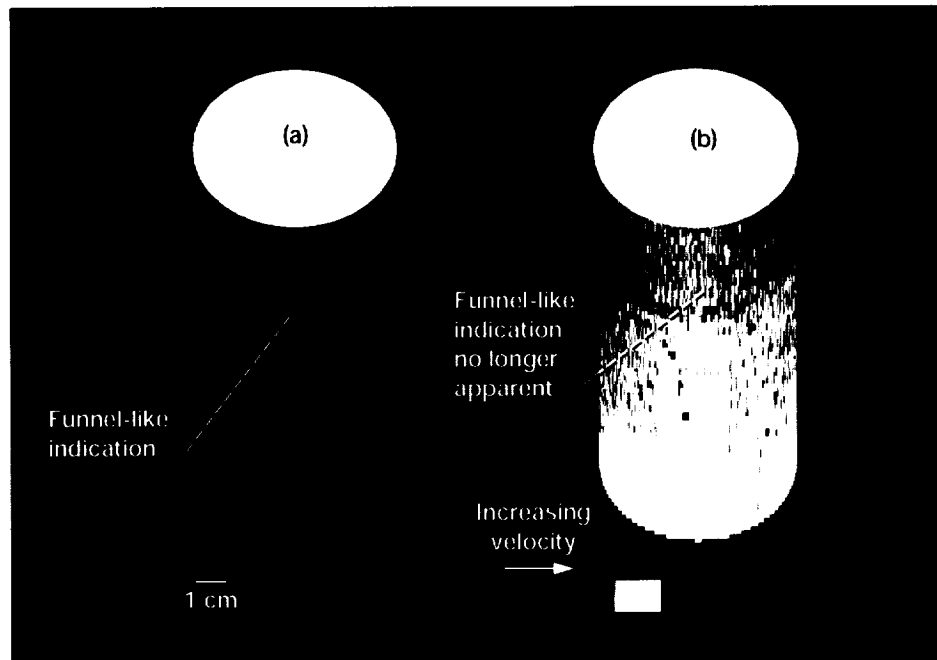


Figure 9.—Apparent and thickness-independent velocity images of silicon nitride tube as decaled onto tubular models. Baseline orientation. (a) Apparent velocity image. (b) Thickness-independent velocity image.

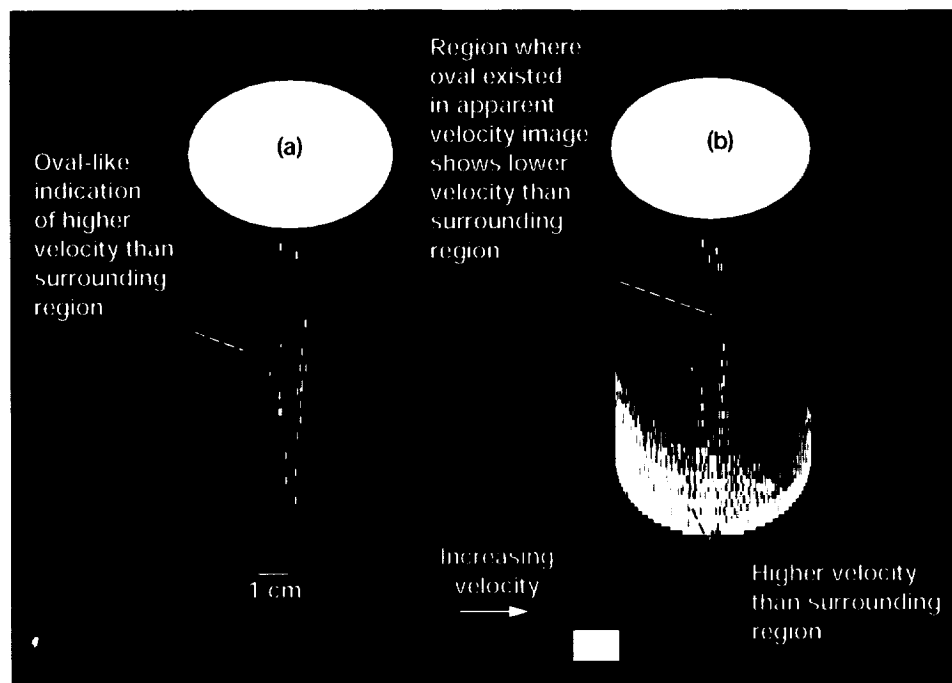


Figure 10.—Apparent and thickness-independent velocity images of silicon nitride tube as decaled onto tubular models. View 180° rotated from baseline orientation. (a) Apparent velocity image. (b) Thickness-independent velocity image.

coarse scan height increment (1 mm) employed and wave interference (diffractive scattering) present at sharp edges. The thickness-independent velocity images of figures 5(b) and 6(b) show all five patches have nearly the same velocity except for some remaining indications around the edges. The surrounding material shows minor velocity versus position variation for both materials. These results on "proof of concept" samples indicate the feasibility of using this technique on monolithic and composite tubular/curved structures.

Silicon Carbide/Silicon Carbide Ceramic Matrix Composite Tube

Figure 7 shows imaging results for an 80 mm height slice of the silicon carbide/silicon carbide ceramic matrix composite (CMC) tube. It was very difficult to gate ultrasonic echoes for this tube due to significant ultrasonic scatter caused by severe surface roughness on both tube surfaces and the fiber weave pattern. The apparent velocity image of figure 7(a) shows indications of both the surface roughness and grooves which both cause thickness variations. Lower-than-average apparent velocity patches are also seen. These regions differ in apparent velocity by ~17 percent from that of the higher-than-average apparent velocity grooved regions. The majority of the indications (including the velocity patches discussed above) in the apparent velocity image are not seen in the thickness-independent velocity image indicating they are due to thickness variations. However, indications of surface roughness and grooving remained in the thickness-independent velocity image and accounted for as much as ~6 percent of the velocity variation. This is possibly due to the surface roughness and grooving (1) causing refractive scattering effects due to nonperpendicular incidence of the ultrasonic beam on the sample or reflector plate surfaces in the M' scan resulting in timing inaccuracies (see Appendix) and/or (2) acting like edges or sharp discontinuities thus causing diffractive effects in both the B1,B2 DTOF and M' scans (similar to the effect created by the sharp patch edges for the ultrasonic images of the mullite and PMC proof-of-concept tubes). The tube was needed for further investigation and could not be destructively analyzed for microstructural variation at the time of this investigation.

Silicon Nitride Tube

Figures 8 to 10 show imaging results for a 130 mm height portion of the silicon nitride tube having a 0.8 mm (10 percent) thickness variation and some microstructural variation. A funnel-like feature showing decreasing velocity from tube bottom-to-top is indicated in the apparent velocity images of figures 8(a) and 9(a). This feature disappears in the thickness-independent unwrapped image of figure 8(b) and decal image of figure 9(b) indicating it was due to thickness variation. Now consider the apparent velocity decal image of figure 10(a) which was rotated 180° (about the height axis) from the view shown in figure 9(a). For this orientation, an oval-like feature is indicated which is ~14 percent greater apparent velocity than that for the funnel-like region. In the thickness-independent decal image of figure 10(b) (which is the same rotational orientation as that of the apparent velocity image decal shown in fig. 10(a)), the region where the oval existed now shows ~3 percent lower velocity than that for the region where the funnel existed. These results indicate that thickness and microstructural variations are present in the tube. The thickness variations in the two regions of the tube (funnel- and oval-like in apparent velocity image) were confirmed in the x-ray computed tomography (CT) slices (0.05 reconstructed pixel size) (fig. 11). (Due to artifacts from beam hardening during the x-ray CT in the 3-radial cross-sectional tube slice configuration, it was not possible from the slice images to draw conclusions regarding inner-to-outer, or top-to-bottom, microstructural variation in the tube.)

Conventional x-ray film radiography and destructive metallographic analysis were used to confirm and determine the nature of the velocity variations seen in the thickness-independent velocity image. Radiography was performed at high and low velocity tube regions (noted on fig. 8(b)) where thicknesses were nearly identical (within 0.8 percent). The film was placed against the inner wall so that the resulting x-rays averaged through the wall thickness. Figure 12 shows the x-ray film radiographs at high and low velocity locations and corresponding x-ray density profiles (eq. (5)). The higher velocity location showed an x-ray density of 2.9 while the lower velocity section showed an x-ray density of 3.02, an ~3 percent difference. The higher x-ray density value indicates more x-rays were received at the film which in turn indicates a more porous, less physically-dense material for the lower velocity section. This result is consistent with prior studies showing (1) ultrasonic velocity to be linearly proportional to physical density for silicon nitride (fig. 1) (ref. 1) and (2) x-ray density to be inversely proportional to physical density for silicon nitride (ref. 19). Metallographic examination of the tube confirmed variable pore fraction throughout

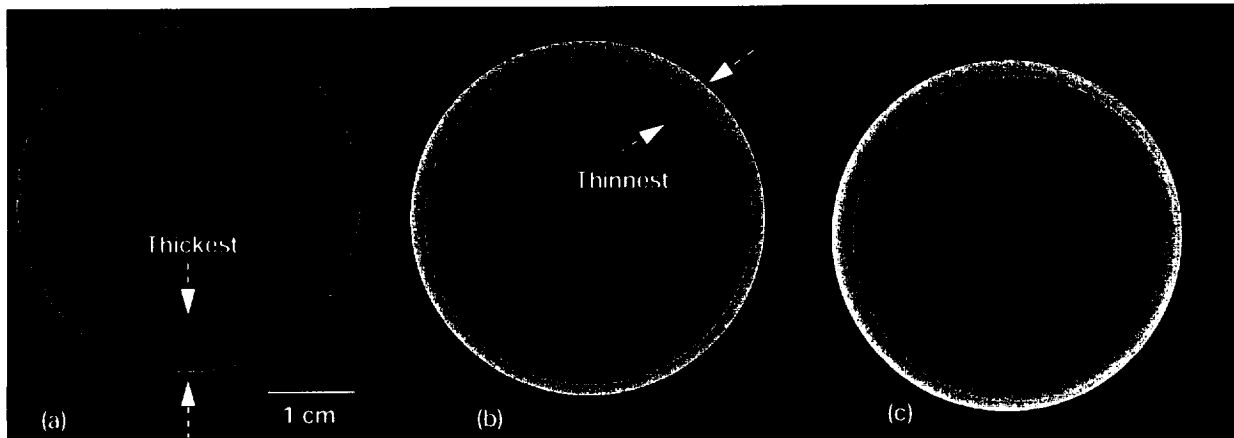


Figure 11.—X-ray computed tomography slices of silicon nitride tube cross-sections at (a) tube top sliced through top of funnel-like indication seen on apparent velocity image; arrows indicate thickest section region which coincides with radial location where funnel-like indication occurred; (b) tube middle sliced through center of oval-like feature seen on apparent velocity image; arrows indicate thinnest section region which coincides with radial location where oval-like indication occurred and is located $\sim 150^\circ$ away from where funnel-like indication higher velocity occurred; (c) tube bottom sliced through location 25 mm up from bottom; thickness is most uniform for this section as compared to those in (a) and (b). Thicknesses were measured directly off of the CT slices. Due to beam hardening effects during the x-ray ct, it was not possible from the slice images to draw conclusions regarding inner-to-outer, or top-to-bottom, microstructural variation in the tube.

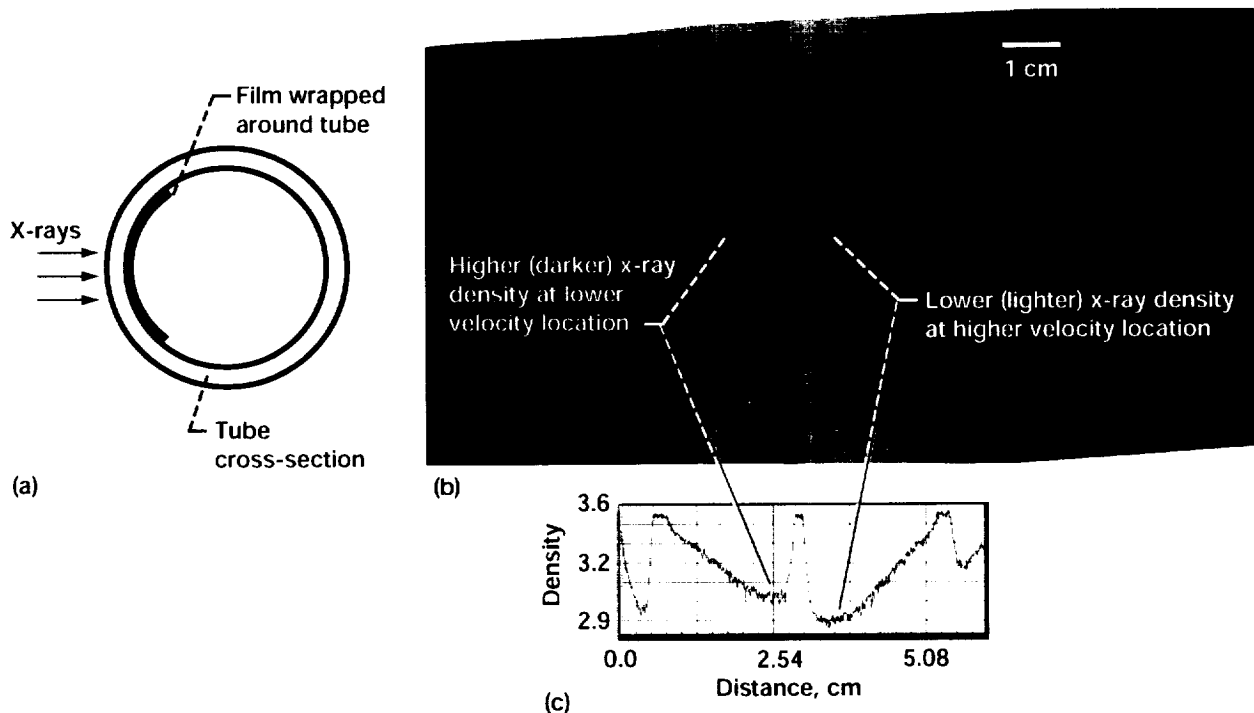


Figure 12.—Conventional x-ray film images (digitized) and x-ray density line profiles at silicon nitride tube locations where higher and lower velocities were seen on thickness-independent velocity image of fig. 8b. (a) Top view schematic of configuration used in x-ray film radiography of silicon nitride tube cross-sections. (b) X-ray images. (c) X-ray line profiles of x-ray images. Sloped, rather than horizontal and vertical, lines are seen on x-ray line profile because silicon nitride cross-sections were curved.

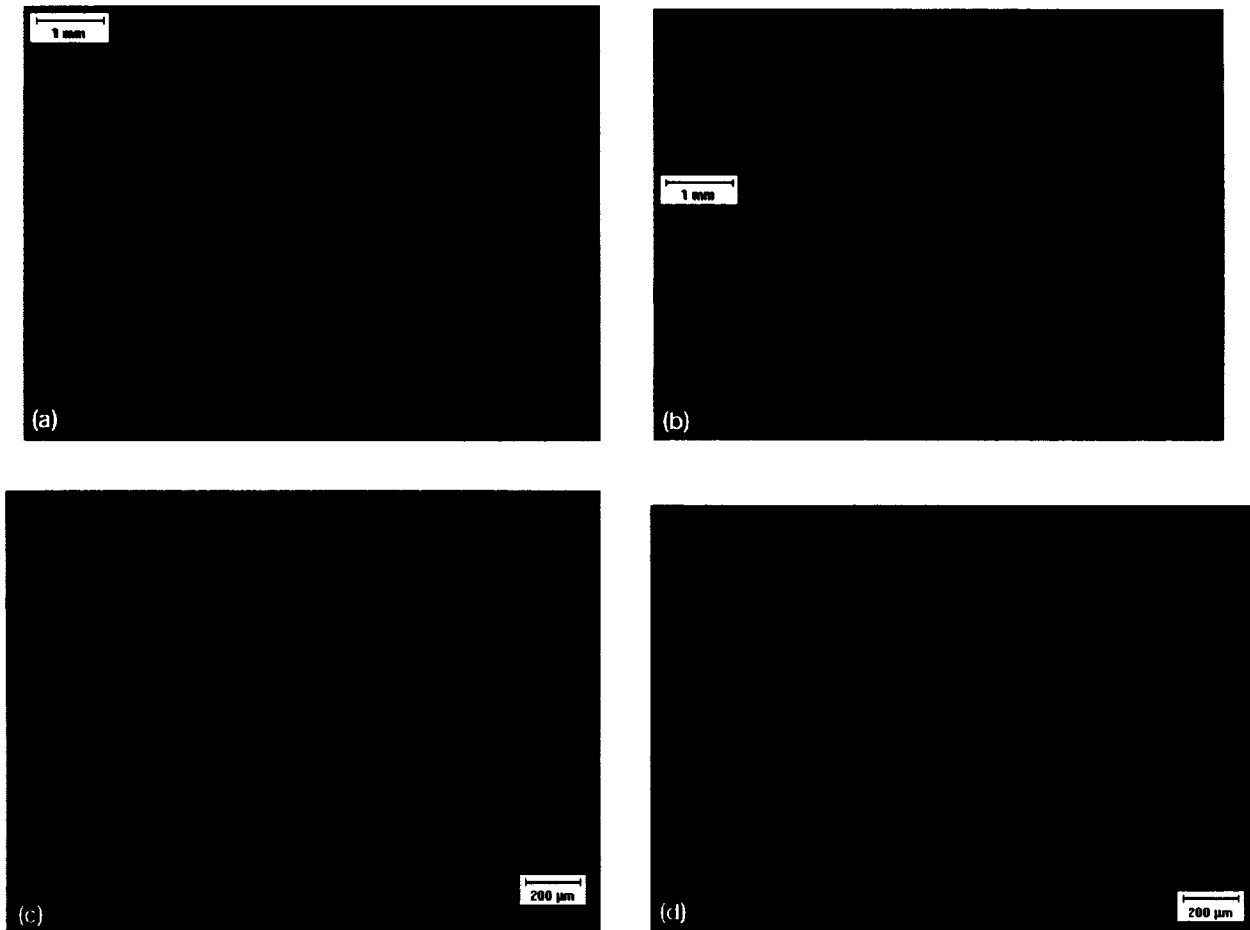


Figure 13.—Optical Micrographs of silicon nitride tube showing variation in density/pore fraction. Dark spots indicate pores. (a) Lower pore fraction location in center of cross-section. (b) Higher pore fraction location in center of cross-section at different location than in (a). (c) Lower pore fraction location at outer edge of cross-section. (d) Higher pore fraction location at outer edge of cross-section at different location than in (c).

the tube (fig. 13). Looking at the cut and polished cross-sectional rings, pore fraction variation can be seen to vary (1) within the center area from cross-sectional location to cross-sectional location (fig. 13(a)) and (2) from outer to inner edge (fig. 13(b)). (The silicon nitride material is actually a multiphase solid composed of β -silicon nitride grains surrounded by a glass phase between the grains. The glass phase percentage was found to be approximately $18 \pm 2\%$ at six locations using backscatter electron microscopy. On the other hand, porosity percentage was found to vary from 0.3 to $2.2 \pm 0.1\%$ at the same six locations, a much more significant variation than for the glass phase. Additionally, porosity variation is likely to have a much more significant impact on velocity than would solid phase variation.)

CONCLUSIONS

Prior studies described a pulse-echo time-of-flight based ultrasonic imaging method that requires using a single transducer in combination with a reflector plate placed behind samples that eliminates the effect of thickness variation in the image. In those studies, this method was successful at isolating ultrasonic variations due to material microstructure in plate-like samples of silicon nitride, metal matrix composite, and polymer matrix composite. In this study, the method is engineered for inspection of more complex-shaped structures—those having (hollow) tubular/curved geometry. The experimental inspection technique and results are described as applied to (1) monolithic multi-lite ceramic and polymer matrix composite “proof-of-concept” tubular structures that contain machined patches of

various depths and (2) as-manufactured monolithic silicon nitride ceramic and silicon carbide/silicon carbide composite tubular structures which might be used in “real world” applications. The method proved highly successful at eliminating gross thickness variation effects in the images of the proof-of-concept tubes, and the silicon nitride “real world” tubes. Moderate success was achieved in eliminating thickness variation effects in the ultrasonic image of the ceramic matrix composite tube in spite of the severe surface roughness that likely caused significant ultrasonic scatter. For the silicon nitride tube, conventional film radiography and destructive metallographic analysis confirmed the presence of microstructurally-different regions first revealed by different velocity indications in the thickness-independent ultrasonic image. The microstructural difference was density/pore fraction which agrees with results from prior studies on silicon nitride and other powder metallurgy products. This technique appears to be quite successful at eliminating the majority of thickness variation effects in curved tubular structures. Edge effects associated with sharp, discontinuous changes in thickness were not completely eliminated. In general, inside and outside surfaces of the tubular structures should be nearly parallel to each other and perpendicular to the impinging ultrasonic beam to avoid refractive effects that lead to reduced accuracy in the resulting velocity image, but some out-of-roundness/nonparallelness of surfaces can be tolerated allowing more practical application as shown in this study. This is a major advantage of the method over peak amplitude-based ultrasonics which are drastically-affected by refractive conditions resulting from out-of-roundness. It is believed that the use of this method can result in significant cost savings because the ultrasonic image, and consequently assessment of tube material and manufacturing quality, can be interpreted correctly in the presence of thickness variations.

APPENDIX—TIMING ISSUES

Time Resolution

Time resolution (TR) of the ultrasonic data acquisition for the commercial scan system employed in this investigation can be defined in terms of analog-to-digital (a/d) sampling rate, gate length in points, and number of gate bits available (time mode) according to:

$$TR(n \text{ sec}) = \left(\frac{1}{\text{sampling rate [GHz]}} \right) \quad (\text{A1a})$$

for 8-bit gate length ≤ 256 points and for 16-bit gate length ≤ 65536 points and

$$TR(n\text{sec}) = \left(\frac{\text{gate length [pts]}}{2^n} \right) \left(\frac{1}{\text{sampling rate [GHz]}} \right) \quad (\text{A1b})$$

for 8-bit gate lengths > 256 points and for 16-bit gate length > 65536 points where n is the number of bits in the gate. Figure A1(a) shows time resolution versus gate length in points under the conditions defined by equations A1(a) to (b).

Alternately, time resolution (TR) of the ultrasonic data acquisition can be defined in terms of analog-to-digital (a/d) sampling rate, gate length in nsec, and number of gate bits available according to:

$$TR(n\text{sec}) = \left(\frac{1}{\text{sampling rate [GHz]}} \right) \quad (\text{A1c})$$

for 8-bit gate, $(\text{a/d sampling rate [GHz]}) \times (\text{gate length [nsec]}) \leq 256$ and for 16-bit gate, $(\text{a/d sampling rate [GHz]}) \times (\text{gate length [nsec]}) \leq 65536$ and

$$TR(n\text{sec}) = \left(\frac{\text{Gate Length (nsec)}}{\text{maximum gate length before resolution degrades (nsec)}} \right) \left(\frac{1}{\text{sampling rate [GHz]}} \right) \quad (\text{A1d})$$

where maximum gate length before resolution degrades (nsec) occurs when: for 8-bit gate, $(\text{a/d sampling rate [GHz]}) \times (\text{gate length [nsec]}) > 256$ and for 16-bit gate, $(\text{a/d sampling rate [GHz]}) \times (\text{gate length [nsec]}) > 65536$. Figure A1(b) shows time resolution versus gate length in nsec under the conditions defined by equations A1(c) to (d).

Figures A1(a) and (b) show the gate lengths where time resolution begins to degrade beyond that set by the a/d sampling rate. *Gate lengths where time resolution begins to degrade beyond that set by the a/d sampling rate are normally never approached in practical scan set-ups when using 16-bit gates.* The 16-bit gate (time mode) was specifically developed to allow longer gates with no decrease in time resolution. For acquisition of echo features for a sample having significant thickness variation, and when using high a/d sampling rates, long gates are normally necessary to follow the echo movement as sample thickness changes. Hence, where long data gate lengths are necessary, it is important to employ 16-bit data gates for highest time resolution. It is also necessary to keep in mind that the commercial scan system employed in this investigation has an 8192 data point acquisition limit; specifically, the first gate starting point subtracted from the last gate ending point must be less than 8192 points.

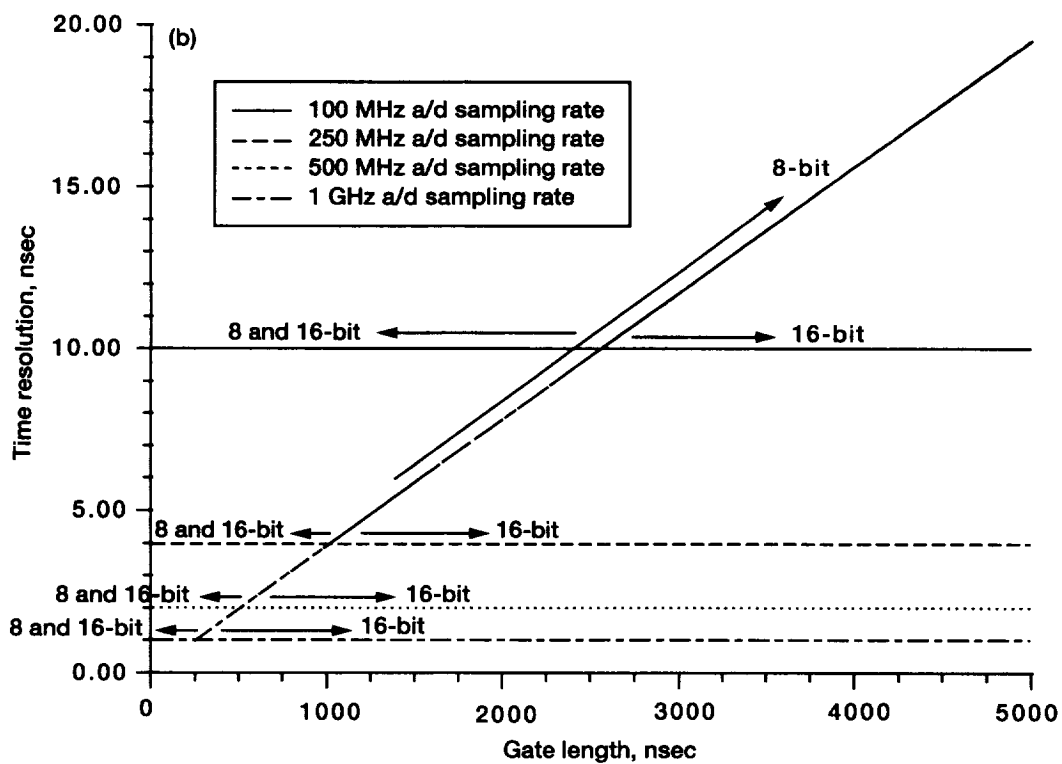
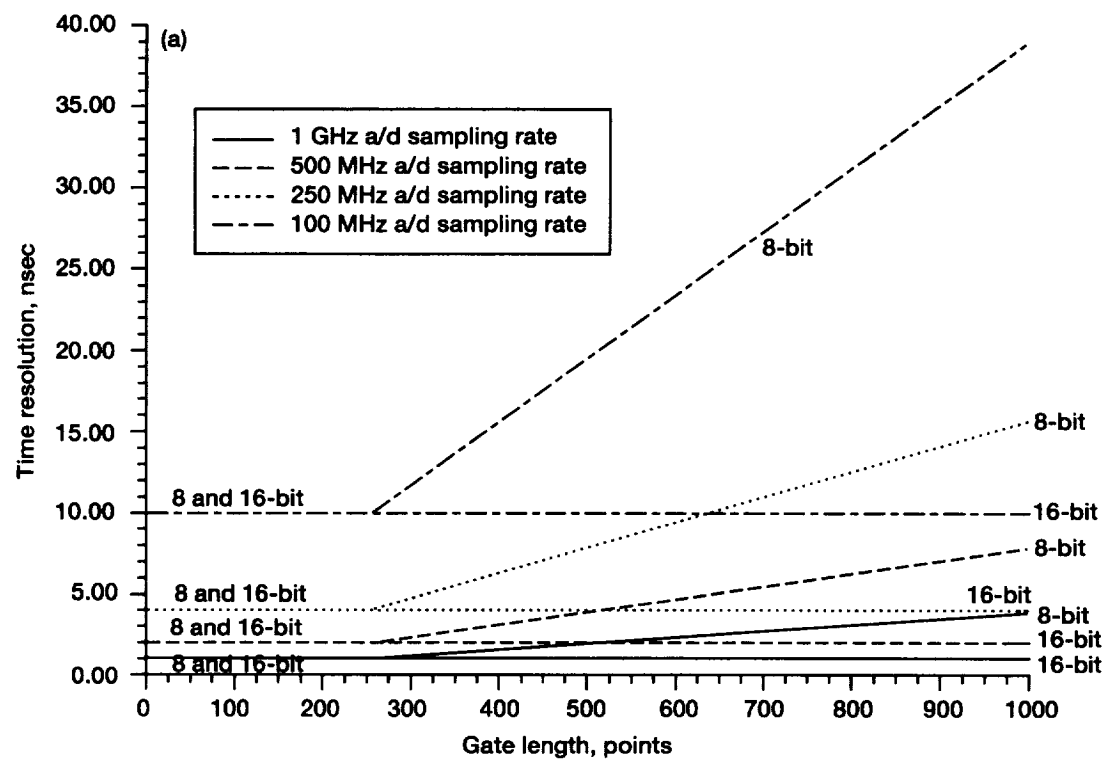


Figure A1.—(a) Time resolution versus gate length in points. (b) Time resolution versus gate length in nsec.

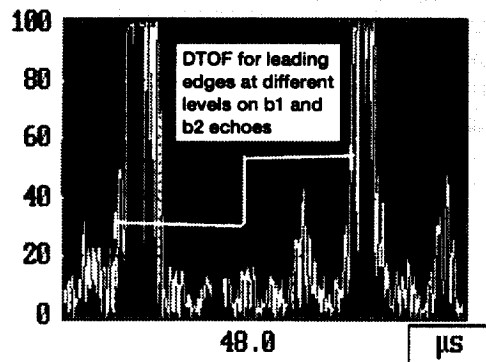
Choice of Timing Methods

A variety of choices regarding time-of-flight (TOF) collection are possible on the commercial scan system used in this investigation. Time-of-flight associated with echo features such as positive and negative peaks, and leading edges, can be acquired during the scan, followed by time delay calculation in real-time or during post-scan processing. Alternately, time delays can be calculated by cross-correlating (ref. A1) echoes during the scan (for B1 and B2), or post-scan from digitized and stored echoes (for B1 and B2, and for M' and M''). Another method related to time delay calculation is the calculation of phase delay in the frequency domain which requires first digitizing and storing all echoes. Using the latter method would result in a phase velocity (velocity at a specific frequency) being calculated from equation (4) and was beyond the scope of this investigation. The optimum time-of-flight collection method to be chosen depends on the characteristics of the waveforms for a particular configuration. These characteristics are affected by transducer features including center frequency and bandwidth, pulser-receiver settings such as gain and damping, and sample microstructural features and thickness. Additionally, it is important to consider the phase relationship of the two echoes for both the sample echoes (FS, B1 or B1, B2) and reflector plate echoes (M', M''). As a result, some experimentation is usually required to determine the optimum time-of-flight collection method. As specific examples, figures A2(a) to (f) show different ultrasonic echoes reflecting off of the front and back surfaces of a silicon nitride sample using a 10 MHz transducer. The features that are sometimes used to calculate the difference in time-of-flight (D_{TOF}, 2τ and Δt in this investigation) between two echoes are illustrated by the horizontal line drawn between two echoes in each figure. In figures A2(a) to (d), echoes B1 and B2 are shown. These echoes are separated by enough time (approximately 0.5 μ sec) such that no interference between them is evident. Additionally, the echoes are in phase with respect to each other. In this situation, the D_{TOF} between the two echoes is best calculated using coincident features via the following possibilities: positive cross-correlation (rf mode), (+)peak_{B1}-to-(+)peak_{B2} (rf mode), (-)peak_{B1}-to-(-)peak_{B2} (rf mode), leading positive edge_{B1}-to-leading positive edge_{B2} for leading edges at 100 percent full-scale height or at coincident positions on the leading edge (rf mode), or absolute peak-to-absolute peak (video mode). In figure A2(e), echoes FS and B1 are shown. These echoes appear to be phase-inverted with respect to each other so that the D_{TOF} between the two echoes is best calculated using opposite echo features via the following: negative cross-correlation, (-)peak_{FS}-to-(+)peak_{B1} (rf mode), (+)edge_{FS}-to-(-)edge_{B1} (rf mode), etc. In figure A2(f), the phase-inverted echoes FS and B1 are shown in video mode. Because the echoes are phase-inverted, calculation of D_{TOF} using leading edge_{B1}-to-leading edge_{B2} at 100 percent full-scale height (%FSH) (video mode) would provide a less accurate absolute velocity than using the D_{TOF} calculated from opposite echo features.

For successive echoes reflecting off sample surfaces (FS, B1, B2, etc.) that are very close together (<0.2 μ sec) because of any combination of transducer frequency, sample thickness, etc., precise gating is required to consistently capture the sought after times to echo peaks or edges. This precise gating can be difficult to maintain throughout an entire scan. For instance, at some scan locations, echoes can slightly interfere (possibly due to change in sample thickness or microstructure as compared to original scan set-up location) and the gate can acquire a time-of-flight associated with an adjacent echo feature due to its nearness. Therefore, for 2τ calculation (where FS and B1, or B1 and B2, are used), cross-correlation is recommended as it appears to be able to consistently "separate" echoes and provides accurate velocity images. For the echoes off the reflector plate, cross-correlation cannot be done during the scan since separate scans are required to collect the necessary time-of-flight information associated with M' and M''. Usually, TOF to the leading edge, (+)peak, or (-)peak of echoes M' and M'' results in the calculation of a valid time delay for Δt .

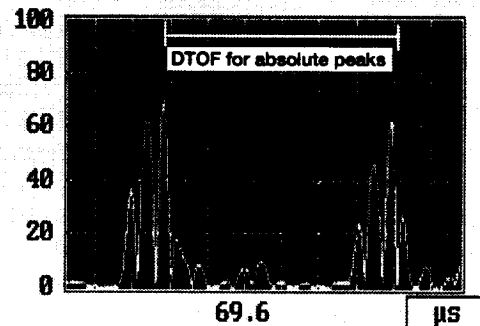
Another TOF-related problem can occur when using the TOF to the "leading" edge at a certain %FSH. Small peaks present before the true leading edge can periodically oscillate above the gate threshold (fig. A3(a)). In this case, the TOF acquired will not be that desired, and the accuracy of the resultant time-of-flight and velocity images will suffer. Figure A3(b) shows a 2τ D_{TOF} (using B1 and B2) image for the silicon nitride ceramic tube where TOF to leading positive edge at ~40 percent FSH (B1) and ~30 percent FSH (B2) was used to calculate D_{TOF}. Note the outstanding D_{TOF} continuous regions on each side of the image. These regions raised immediate suspicion as to validity since they differed in velocity by nearly 10 percent from surrounding regions, and in fact were due to undesired initial positive B1 peaks periodically oscillating to 50 percent FSH. This situation can usually be avoided by raising the pulser-receiver gain so that the echoes' leading edges consistently saturate at 100 percent FSH and gating either the positive or negative leading edge of the waveform at or near 100 percent FSH, and/or gating the positive or negative leading edge which displays the least defined prior small peaks. Another method that will generally avoid acquisition of undesired D_{TOFs} is echo cross-correlation. The correct 2τ D_{TOF} image is shown in

2FSH Video mode, b1 and b2 are in phase



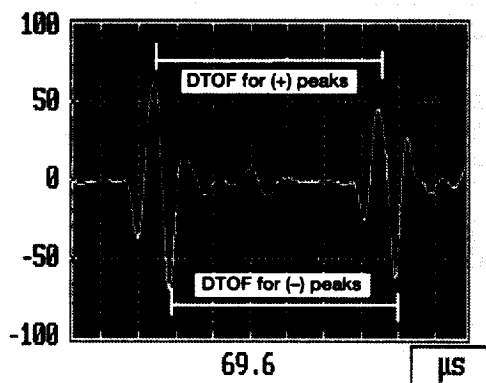
(a)

2FSH Video mode, b1 and b2 are in phase



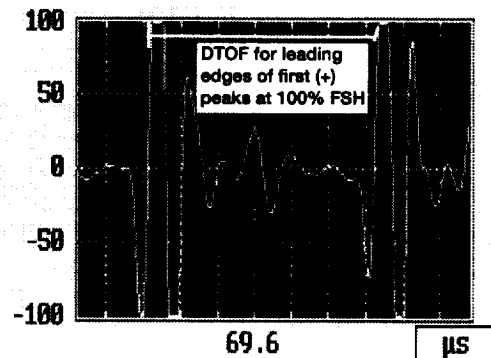
(b)

2FSH RF mode, b1 and b2 are in phase



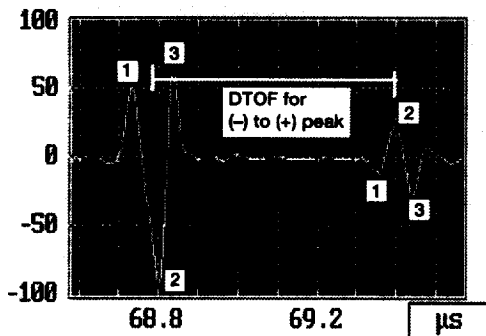
(c)

2FSH RF mode, b1 and b2 are in phase



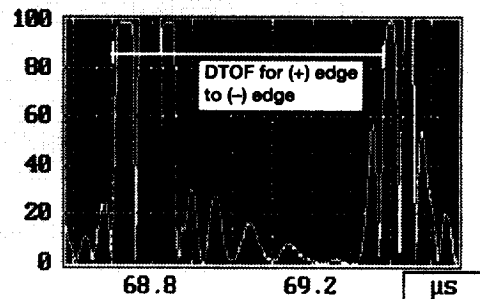
(d)

2FSH RF mode, fs and b1 phase reversed



(e)

2FSH Video mode, fs and b1 phase reversed



(f)

Figure A2.—Illustration of echo features that can be used in collection of time of flight difference (DTOF) between two echoes. (a) Video mode, B1 and B2 are in phase, collect times to leading edges of echoes at different levels so that coincident features are collected. (b) Video mode, B1 and B2 are in phase, collect times to absolute peaks. (c) RF mode, B1 and B2 are in phase, collect times to either coincident (+) or (-) peaks. (d) Video mode, B1 and B2 are in phase, collect times to leading edges at 100% FSH. (e) RF mode, FS and B1 are phase-reversed, numbers 1,2,3 indicate coincident echo peaks, collect times to (-) peak of FS and (+) peak of B1. (f) Video mode, FS and B1 phase reversed, collect times to (+) edge for FS and what is really (-) edge for B1 if it was displayed in RF mode.

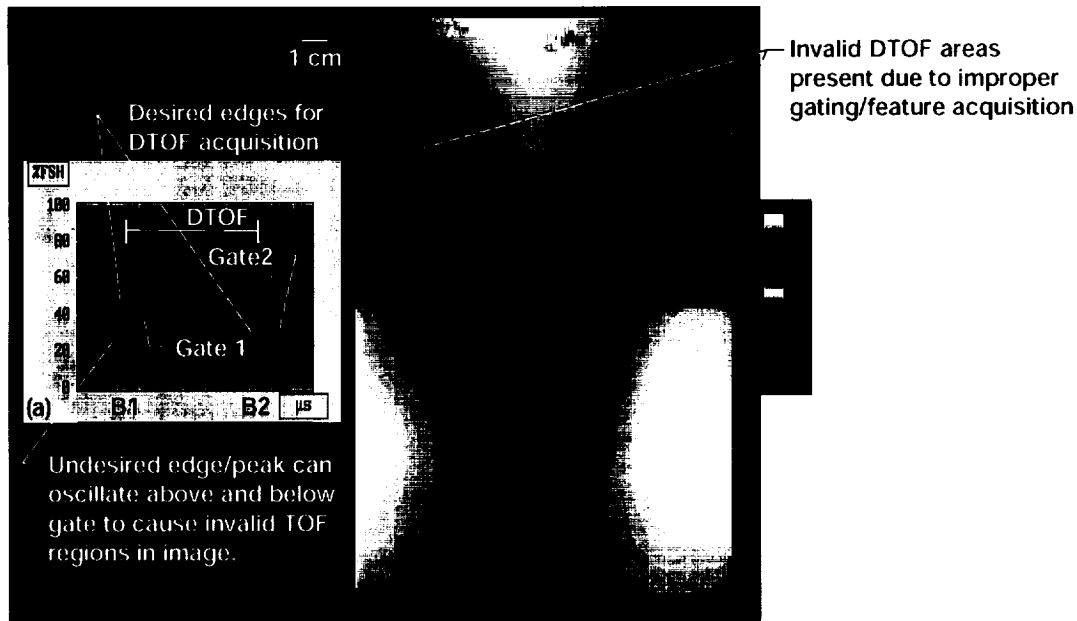


Figure A3.—Gating and two DTOF (B1, B2) ultrasonic images for silicon nitride tube. (a) Gate and feature acquisition set-up. In this gating scheme, the intersection of gate with leading edge of 2nd peak was attempted for both B1 and B2. (b) Resulting image with improper gating/echo feature acquisition. At some scan locations, the 1st peak of B2 increased in height and intersected the gate so that DTOF was improperly decreased. (c) Resulting image with proper gating/echo feature acquisition. The color scheme chosen best illustrated the invalid TOF regions.

figure A3(c) where cross-correlation of B1 and B2 was performed. Note that the outstanding DTOF continuous regions are not apparent in this image.

An additional issue with regards to phase is important to note. Phase inversions of one echo with respect to another (example B1, B2), not the norm for a particular sample and scan set-up, may occur at some scan locations due to interaction of ultrasound with discrete volumetric or surface flaws. Because the majority of the echoes are in-phase with respect to one another, if cross-correlation for example was the preferred DTOF method, positive correlation would be the correct choice of calculation methods. However, in those scan locations where phase inversion occurs, positive cross-correlation will produce incorrect values for the time delay. It has been found for a silicon nitride sample that such incorrect correlation will produce a value of DTOF that is ~7 percent different (less accurate) than that where correct correlation is performed. Such values may show up as extreme high or low velocity values in the velocity image and should be filtered out if possible.

Refractive Effects

In general, tubular structures can be difficult to inspect in the pulse-echo mode in a scan array fashion if the tube is out-of-round at some locations. This is because ultrasound bends, or refracts, when impinging upon surfaces that are not orthogonal/perpendicular to it. Parallelism between inside and outside surfaces of the tubular structures, and perpendicular incidence of the impinging ultrasonic beam on the sample surfaces and reflector plate, is important to avoid refractive effects that lead to reduced accuracy in the resulting velocity image (ref. A2). A preliminary experiment was performed to examine refractive effects using a silicon nitride monolithic ceramic wedge plate. The plate was machined on one surface to produce a 0.3 mm thickness gradient over an approximate 35 mm length resulting in an ~0.5° incline angle between the plate surfaces. Figure A4 shows three-dimensional representations of the apparent velocity and thickness-independent ultrasonic velocity images for the plate. It can be seen by comparing the images that the thickness variation effect is eliminated in the thickness-independent image, so only minor

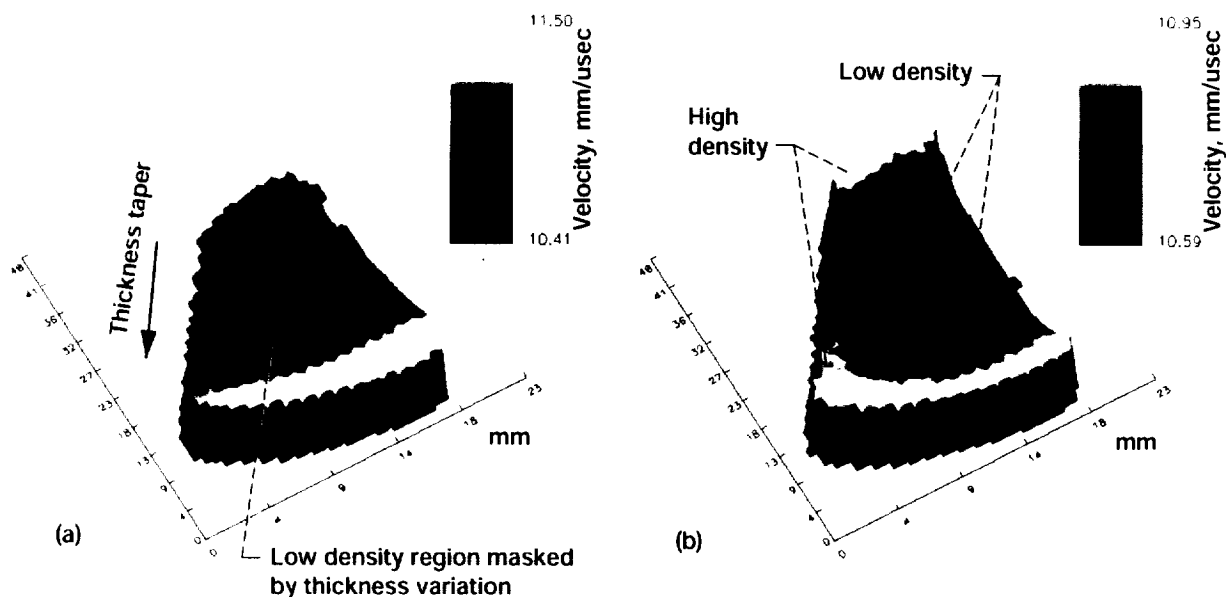


Figure A4.—3d representations of apparent and thickness-independent velocity images of silicon nitride ceramic wedge plate having 0.5° slope. (a) Apparent velocity image. (b) Thickness-independent velocity image.

error due to refractive effects is likely. Velocity values obtained in the thickness-independent image agree within 1 percent of those obtained from contact measurements.

The following additional experiments were performed to investigate the effect of change in ultrasonic beam incidence angle (simulating surface nonparallelness/out-of-roundness) on echo TOFs, DTOFs, Velocities (V) and peak amplitudes (PAs). Incidence angle was changed by changing the gimbal (up and down motion in the vertical direction (ZX plane)) and swivel (left to right sideways motion in the horizontal direction (XY plane)) angular positions of the transducer (fig. 3). The mullite tube was employed for these experiments. 20 MHz longitudinal wave spherically-focused transducer and 1 GHz analog-to-digital sampling rate (giving 1 nsec time resolution) were used. The (+)peak was used as the echo feature for which the time measurements were based on. Percentage changes (%Δ) in echo TOF, DTOF, V and PA were calculated from:

$$\% \Delta \text{Property} = 100 \left(\frac{|B - X|}{B} \right) \quad (\text{A2})$$

where B is the baseline (initial) position value and X is the value at the specific angular position. Tables AI and AII provide the results of these experiments. The reader should focus on the bolded values which show changes in time-of-flight, velocity, and peak amplitude as a result of gimbal and swivel changes. B1 and B2 echoes were reduced to near 0 percent FSH for gimbal and swivel angle changes beyond those shown in the table so that the effect of larger angle changes could not be determined. Water velocity = 1.48 mm/μsec was used to calculate velocity (eq. (4)).

These results show that (1) changes tend to be consistent, i.e., $\% \Delta B1 \cong \% \Delta B2$ for TOF and PA changes, (2) TOF, DTOF and Velocity change insignificantly (<0.5 percent) with changes in gimbal angles less than ~5 deg, (3) TOF, DTOF and Velocity change insignificantly with changes in swivel angles less than ~0.3 deg which was the largest swivel angle change possible; (4) PA generally changes drastically (70 to 100 percent) with changes in gimbal and swivel angles, and (5) small swivel angle (sideways) changes result in significantly more dramatic changes in PA than do small gimbal angle changes. Figure A4 and points (2) and (3) just stated indicate that TOF-based

TABLE A1.—THE EFFECT OF CHANGE IN GIMBAL ANGLE ON TIME-OF-FLIGHT AND PEAK AMPLITUDE BASED MEASUREMENTS

Change in Gimbal angle from baseline, degree	%Δ TOF (%ΔB1 and %ΔB2), %Δ DTOF (%Δ(2τ) and %Δ(Δt)), and %Δ V							%Δ Peak amplitude			
	%ΔB1	%ΔB2	%Δ(2τ)	%Δ(M')	%ΔM''	%Δ(Δt)	%Δ V	%ΔB1	%ΔB2	%ΔM'	%ΔM''
5.16	0.33	0.32	0.03	0.42	0.35	0.22	0.15	71.11	63.20	86.92	78.79

TABLE A2.—THE EFFECT OF CHANGE IN SWIVEL ANGLE ON TIME-OF-FLIGHT AND PEAK AMPLITUDE BASED MEASUREMENTS

Change in Swivel angle from baseline, degree	%Δ TOF (%ΔB1 and %ΔB2), %Δ DTOF (%Δ(2τ) and %Δ(Δt)), and %Δ V							%Δ Peak amplitude			
	%ΔB1	%ΔB2	%Δ(2τ)	%Δ(M')	%ΔM''	%Δ(Δt)	%Δ V	%ΔB1	%ΔB2	%ΔM'	%ΔM''
0.32	0.02	0.02	0.16	0.03	0.03	0.06	0.08	73.30	72.89	12.33	9.22

ultrasonic images of tubular samples having some out-of-roundness/nonparallelness of surfaces will contain only small error if echoes are still measurable. Points (4) and (5) just stated lead one to conclude that *because of the severe effect that out-of-roundness has on peak amplitude, it is difficult to interpret the results of peak amplitude c-scans where backwall echoes are gated for tubular structures. This effect will be essentially severe for small tubes or curved structures having tight radii.* Based on these experiments, it is the opinion of the authors that peak amplitude c-scans of curved structures may not be accurate unless carefully setting up for continuous perpendicular incidence of the ultrasonic beam on the structure surface, and/or parallel structure surfaces. At locations in a real tubular sample exhibiting out-of-roundness/nonparallelness of surfaces such that echoes are reduced to below gate thresholds in a TOF-based scan, it is suggested that an average of nearest neighbors is used at those locations to provide a continuous TOF/DTOF/V image.

Mechanical Stability of Turntable

The mechanical stability of the turntable is based on the quality of the drive mechanism, including the bearings, chain, and gearing. Nonuniformity such as bearing high spots will cause a "rocking" motion in the turntable which may be indistinguishable by eye but can be seen on the oscilloscope by (1) watching reflected echoes oscillating back and forth along the time axis and (2) in the resultant rf b-scan where a triangular wave pattern indicates this back and forth echo motion. As an example of (2), figure A5(a) shows an approximate 0.4 μsec peak-to-peak "jitter" in the rf b-scan of the M' echo for a situation where some substantial rocking is present in the turntable drivetrain. In contrast, figure A5(b) shows an approximate 0.2 msec peak-to-peak "jitter" in the rf b-scan of the M' echo for a situation where minimal rocking is present in the turntable drivetrain. This situation becomes a major issue when attempting to measure precise time delays associated with the reflector echoes M' and M''. In the best case scenario if rocking is present, if "perfect" positional relative alignment is present between the M' and M'' scans and no refraction during the M' scan is caused by tube out-of-roundness condition, the jitter/timing errors caused by turntable rocking would be cancelled out in the Δt DTOF calculation since $\Delta t = TOF_{M''} - TOF_{M'}$. In the worst case scenario if rocking is present, perfect positional relative alignment is not present between the M' and M'' scans, and refraction does occur due to tube out-of-roundness condition, microstructural variation in the tube may be masked by the inaccuracies in measuring echo timing. Obviously, it is advisable to perform TOF-based scanning with the highest quality drive mechanism possible.

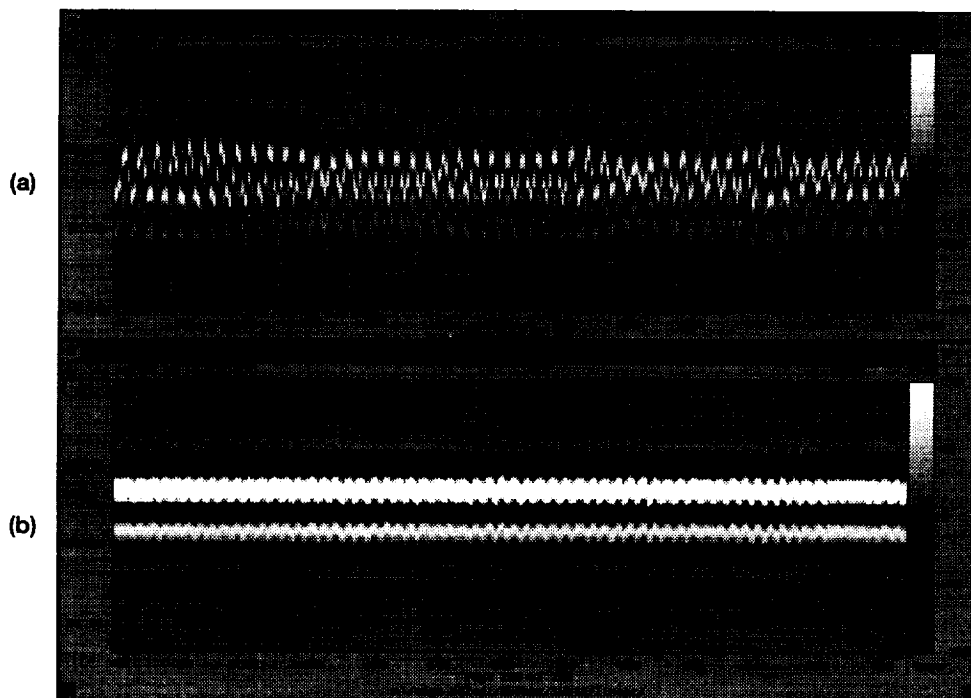


Figure A5.—RF b-scans illustrating (a) rocky and (b) smooth turntable drive mechanism.

REFERENCES

1. Roth, D.J., Stang, D.B., Swickard, S.M., DeGuire, M.R., and Dolhert, L.E.: "Review, Modeling and Statistical Analysis of Ultrasonic Velocity-Pore Fraction Relations in Polycrystalline Materials," **Mater. Eval.**, Vol. 49, No. 7, July 1991, pp. 883–888.
2. Roth, D.J., DeGuire, M.R., Dolhert, L.E. and Hepp, A.F.: "Spatial Variations in a.c. susceptibility and microstructure for the $\text{YBa}_2\text{Cu}_3\text{O}_{7-x}$ superconductor and their correlation with room-temperature ultrasonic measurements," **J. Mater. Res.** 6[10] pp. 2041–2053 (1991).
3. Roth, D.J., et. al.: Quantitative Mapping of Pore Fraction Variations in Silicon Nitride Using an Ultrasonic Contact Scan Technique. **Res. Nondestr. Eval.**, Vol. 6, 1995, pp. 125–168.
4. Roth, D.J.; Baaklini, G.Y.; Sutter, J.K.; Bodis, J.R.; Leonhardt, T.A. and Crane, E.I.: An NDE Approach For Characterizing Quality Problems in Polymer Matrix Composites. **Proceedings of the 40th International SAMPE Symposium**, May 8–11, 1995, pp. 288–299.
5. Roth, D.J., Kautz, H., Draper, S., Bansal, N., Bowles, K., Bashyam, M., and Bishop, C.: "NDE Approaches for Characterization of Microstructural Variations in Ceramic and Metal Matrix Composites," **Proceedings 1993 HITEMP conference**, Oct. 25–27, 1993, Cleveland, Ohio.
6. Christensen, R.M.: *Mechanics of Composites*, John Wiley & Sons, 1979, pp. 47, 51 and 52.
7. Flynn, D.R.: Thermal Conductivity of Ceramics, **Proceedings of Mechanical and Thermal Properties of Ceramics Symposium**, April 1–2, 1968, pp. 92–93.
8. Bowles, K., et.al.: Void Effects on the Interlaminar Shear Strength of Unidirectional Graphite-Fiber-Reinforced Composites. **J. Comp. Mat.**, Vol. 26, No. 10, 1992, pp. 1487–1509.
9. Gruber, J.J., Smith, J.M., and Brockelman, R.H.: Ultrasonic Velocity C-scans for Ceramic and Composite Material Characterization. **Mater. Eval.**, Vol. 46, No. 1, 1988, pp. 90–96.
10. Sollish, B.D.: Ultrasonic Velocity and thickness gage, United States Patent No. 4,056,970, Nov. 8, 1977.
11. Pichè, L.: Ultrasonic velocity measurement for the determination of density in polyethylene. **Polymer Engineering and Science**, Vol. 24, No. 17, Mid-December 1984, pp. 1354–1358.
12. Kuo, I.Y., Hete, B. and Shung, K.K.: A novel method for the measurement of acoustic speed. **J. Acoust. Soc. Am.** Vol. 88, No. 4, Oct. 1992, pp. 1679–1682.

13. Hsu, D.K. and Hughes, M.S.: Simultaneous ultrasonic velocity and sample thickness measurement and application in composites. **J. Acoust. Soc. Am.** Vol. 92, No. 2, Pt. 1, Aug. 1992, pp. 669–675.
14. Dayal, V.: An Automated Simultaneous Measurement of Thickness and Wave Velocity by Ultrasound, **Experimental Mechanics**, September, 1992, Vol. 32 No. 2, pp. 197–202.
15. Hughes, M.S. and Hsu, D.K.: An automated algorithm for simultaneously producing velocity and thickness images, **Ultrasonics**, 1994 Vol. 32 No. 1, pp. 31–37.
16. Roth, D.J.: Using a Single Transducer Ultrasonic Imaging Method to Eliminate the Effect of Thickness Variation in the Images of Ceramic and Composite Plates, **J. Nondestruct. Eval.**, Vol. 16, No. 2, June 1997.
17. Roth, D.J., et. al.: Commercial Implementation of Ultrasonic Velocity Imaging Methods via Cooperative Agreement Between NASA Lewis Research Center and Sonix, Inc. NASA TM–107138, 1996.
18. Nondestructive Testing Handbook, second edition, Volume 7 Ultrasonic Testing, eds. Birks, A.S., Green, R.E., and McIntire, P. American Society For Nondestructive Testing, 1991, pp. 227–230 and 237.
19. Sanders, W.A. and Baaklini, G.Y.: “Correlation of Processing and Sintering Variables with the Strength and Radiography of Silicon Nitride,” **Advanced Ceramic Materials**, Vol. 3, No. 1, 1988, pp. 88–94.
20. Palanichamy, P., Joseph, A., Jayakumar, T. and Raj, Baldev, “Ultrasonic velocity measurements for estimation of grain size in austenitic stainless steel,” **NDT & E International**, Vol. 28, No. 3, 1995, pp. 179–185.

APPENDIX REFERENCES

- A1. Hull, D.R.; Kautz, H.E.; and Vary, A.: Measurement of Ultrasonic Velocity Using Phase-Slope and Cross-Correlation Methods. **Mater. Eval.**, Vol. 43, No. 11, 1985, pp. 1455–1460.
- A2. Chu, Y.C. and Rokhlin, S.I.: Comparative analysis of through-transmission ultrasonic bulk wave methods for phase velocity measurements in anisotropic materials, **J. Acoust. Soc. Am.** Vol. 95, No. 6, June 1994, p. 3205.

REPORT DOCUMENTATION PAGE			Form Approved OMB No. 0704-0188	
Public reporting burden for this collection of information is estimated to average 1 hour per response, including the time for reviewing instructions, searching existing data sources, gathering and maintaining the data needed, and completing and reviewing the collection of information. Send comments regarding this burden estimate or any other aspect of this collection of information, including suggestions for reducing this burden, to Washington Headquarters Services, Directorate for Information Operations and Reports, 1215 Jefferson Davis Highway, Suite 1204, Arlington, VA 22202-4302, and to the Office of Management and Budget, Paperwork Reduction Project (0704-0188), Washington, DC 20503.				
1. AGENCY USE ONLY (Leave blank)		2. REPORT DATE February 1998		3. REPORT TYPE AND DATES COVERED Technical Memorandum
4. TITLE AND SUBTITLE Scaling up the Single Transducer Thickness-Independent Ultrasonic Imaging Method for Accurate Characterization of Microstructural Gradients in Monolithic and Composite Tubular Structures			5. FUNDING NUMBERS WU-523-21-13-00	
6. AUTHOR(S) Don J. Roth, Dorothy V. Carney, George Y. Baaklini, James R. Bodis and Richard W. Rauser				
7. PERFORMING ORGANIZATION NAME(S) AND ADDRESS(ES) National Aeronautics and Space Administration Lewis Research Center Cleveland, Ohio 44135-3191			8. PERFORMING ORGANIZATION REPORT NUMBER E-11069	
9. SPONSORING/MONITORING AGENCY NAME(S) AND ADDRESS(ES) National Aeronautics and Space Administration Washington, DC 20546-0001			10. SPONSORING/MONITORING AGENCY REPORT NUMBER NASA TM-1998-206625	
11. SUPPLEMENTARY NOTES Don J. Roth, Dorothy V. Carney, and George Y. Baaklini, NASA Lewis Research Center; James R. Bodis and Richard W. Rauser, Cleveland State University, Cleveland, Ohio 44115. Responsible person, Don J. Roth, organization code 5920, (216) 433-6017.				
12a. DISTRIBUTION/AVAILABILITY STATEMENT Unclassified - Unlimited Subject Category: 38 This publication is available from the NASA Center for AeroSpace Information, (301) 621-0390.			12b. DISTRIBUTION CODE	
13. ABSTRACT (Maximum 200 words) Ultrasonic velocity/time-of-flight imaging that uses back surface reflections to gauge volumetric material quality is highly suited for quantitative characterization of microstructural gradients including those due to pore fraction, density, fiber fraction, and chemical composition variations. However, a weakness of conventional pulse-echo ultrasonic velocity/time-of-flight imaging is that the image shows the effects of thickness as well as microstructural variations unless the part is uniformly thick. This limits this imaging method's usefulness in practical applications. Prior studies have described a pulse-echo time-of-flight-based ultrasonic imaging method that requires using a single transducer in combination with a reflector plate placed behind samples that eliminates the effect of thickness variation in the image. In those studies, this method was successful at isolating ultrasonic variations due to material microstructure in plate-like samples of silicon nitride, metal matrix composite, and polymer matrix composite. In this study, the method is engineered for inspection of more complex-shaped structures—those having (hollow) tubular/curved geometry. The experimental inspection technique and results are described as applied to (1) monolithic mullite ceramic and polymer matrix composite "proof-of-concept" tubular structures that contain machined patches of various depths and (2) as-manufactured monolithic silicon nitride ceramic and silicon carbide/silicon carbide composite tubular structures that might be used in "real world" applications.				
14. SUBJECT TERMS Ultrasonics; Nondestructive evaluation; Velocity; Thickness; Ceramics; Composites; Polymers; Metals			15. NUMBER OF PAGES 33	
			16. PRICE CODE A03	
17. SECURITY CLASSIFICATION OF REPORT Unclassified	18. SECURITY CLASSIFICATION OF THIS PAGE Unclassified	19. SECURITY CLASSIFICATION OF ABSTRACT Unclassified	20. LIMITATION OF ABSTRACT	